

FLORIDA STATE UNIVERSITY
COLLEGE OF ARTS AND SCIENCES

STUDY OF THE REACTION

$$\gamma p \rightarrow \eta' \eta p$$

By

JASON BARLOW

A Dissertation submitted to the
Department of Physics
in partial fulfillment of the
requirements for the degree of
Doctor of Philosophy

2023

Jason Barlow defended this dissertation on July 7th, 2023.

The members of the supervisory committee were:

Paul Eugenio
Professor Directing Dissertation

Ettore Aldrovandi
University Representative

Alexander Ostrovidov
Committee Member

Volker Crede
Committee Member

Jorge Piekarewicz
Committee Member

Harrison Prosper
Committee Member

The Graduate School has verified and approved the above-named committee members, and certifies that the dissertation has been approved in accordance with university requirements.

To mom and dad

ACKNOWLEDGMENTS

The journey of a PhD is long and cumbersome and cannot be achieved without support by family and friends. First of all, I would like to thank my dad and my mom for always believing in me and supporting me. I appreciate both of you listening to all my complaints and struggles along the way and reminding me not to work too hard and that there are more important things to life than studies and school. I'd like to also thank all of my friends for many fun times as well as help in the office when I needed it. Edmundo, you have been my best friend as well as my most valued colleague. We have have been through many tough times together, both academically and personally. I know I wouldn't have made it to the end without your support. Trina, you are a great partner and good listener. You've helped me with various coding problems and also kept life interesting, exploring new places and going on fun trips. I'd like to thank my roommates present and past for plenty of game nights and social events that helped make the work/life balance possible. In particular, Juan Pablo you brought life to the end of some dark times during covid by bringing your enthusiasm for party and fun to many of us. I'd like to also thank my roommate's cat for always greeting me every day when I got home and reminding me that he should be my main focus of attention in life. I'd like to thank my best friends around the world for all the love they have given me. Namely, Arielle (and her entire family), Ashley, and Josh. I want to thank my physics cohort and friends with whom I have shared many memories. The list is long, so if I have missed your name you know you are mentioned here. Dan, Sean, Melissa, Kyle, Luz, Muti, Ryan, Gabe, Nizar, Saheli, Donavan, Lawrence, Jing, Honey, Redwan, Bal, Jake, Angelica, Masoud, and the list goes on, thank you all so much. Professionally, I would like to thank my advisor for all the support and guidance along the way. I'd also like to thank Sasha for his thought provoking questions and curiosity that pushed me to deepen my understanding. I'd like to thank Professor Sean Dobbs and Professor Justin Stevens for their thorough guidance and insight into many challenges along the way. Finally, I'd like to thank my advisory committee for all of their help and for making time to sit in on my defense even though it's scheduled during a holiday week. I could not have succeeded without all of you mentioned above (and many more) and I look forward to keeping touch with everyone in the future.

TABLE OF CONTENTS

List of Tables	viii
List of Figures	ix
List of Abbreviations	xv
Abstract	xvi
1 Introduction	1
1.1 Brief History of Particle Physics	1
1.1.1 Electrons, Protons, and Neutrons: Classical Origins	1
1.1.2 Photons	2
1.1.3 Mesons	3
1.2 Modern Particle Physics	3
1.2.1 The Standard Model	3
1.2.2 Quantum Chromodynamics (QCD)	5
1.3 The Classical Quark Model	7
1.3.1 Symmetries	7
1.3.2 Selection Rules	7
1.4 Exotic & Hybrid Mesons	9
1.5 Motivation	10
1.5.1 The $\pi_1(1600)$	11
1.5.2 The Hypothesized η_1	11
1.5.3 The $\eta_1(1855)$ at BES III	12
2 The GlueX Experiment	14
2.1 Overview of Jefferson Lab	14
2.2 CEBAF	14
2.2.1 Injector	14
2.2.2 RF Linear Accelerators and Linac	17
2.3 Photon Beam	17
2.3.1 Diamond Radiator	17
2.3.2 Photon Tagging	18

2.3.3	Triplet Polarimeter	18
2.3.4	Pair Spectrometer	19
2.4	GlueX Spectrometer	19
2.4.1	Solenoid	19
2.4.2	Target and Start Counter	20
2.4.3	Charged Particle Tracking	22
2.4.4	Electromagnetic Calorimeters	23
2.4.5	Time of Flight	24
2.4.6	Detection of Internally Reflected Cherenkov Light Detector	26
3	Monte Carlo Simulation for $\gamma p \rightarrow \eta' \eta p$	27
4	Data Selection	31
4.1	Kinematic Fitting	32
4.2	Stage 1	32
4.3	Stage 2	40
4.4	Stage 3	42
4.5	Stage 4	43
4.6	Stage 5	46
4.7	Stage 6	48
4.8	Stage 7	50
4.8.1	$\gamma p \rightarrow \eta' \eta p$	52
5	Observable: Cross Section Estimation	55
5.1	Yields	56
5.2	Target Factor	57
5.3	Flux	57
5.4	Branching Fraction	58
5.5	Monte Carlo Efficiency	58
5.6	Differential Cross Section	59
6	Systematics	61
6.1	The Barlow Test of Significance	61
6.1.1	Systematic Study of the Selection of Two η s	61
6.1.2	Systematic Study of the Selection of η'	63

6.1.3 Systematic Study of the Removal of the N(1535)	63
7 Future Outlook and Conclusion	67
Bibliography	69
Biographical Sketch	73

LIST OF TABLES

1.1	Lepton generations with their corresponding charge, electron, muon, and tau numbers [1]	4
1.2	Classification of quarks with their corresponding charge, downness, upness, strangeness, charm, beauty, and top numbers [1]	4
4.1	Run periods with their run range for the GlueX Phase-I data.	31
6.1	Table of systematics for each mass bin and variation where Δ/σ_Δ , the significance, is either greater than 4 or less than -4. σ_Δ is the difference between the differential cross section of the variation and the nominal in units of microbarns/ GeV^2	65

LIST OF FIGURES

1.1	This diagram illustrates the standard model of particle physics. Quarks are represented with purple, leptons are represented with green, and gauge bosons are in orange and yellow [2].	5
1.2	The coupling constant $\alpha_s(Q)$ as a function of the momentum transfer Q . Theoretical predictions are given by the line and the points give the experimental results. Reproduced from [3].	6
1.3	Given here are the SU(4) weight diagrams for the $l = 0$ pseudoscalar meson (a) and vector meson (b) multiplet. The nonet structures are the highlighted planes in the center of the 16-plet. They are arranged based on strangeness, charge, and isospin [4]	8
1.4	Lattice QCD predictions for isoscalar (green and black) and isovector (blue) mesons. Vertical height of each box gives statistical uncertainty of the mass. States outlined in orange are the lowest-lying states having dominant overlap with operators featuring a chromomagnetic construction. Source: Fig. 11 of Ref. [5]	10
1.5	The $M(\eta'\pi)$ from the COMPASS, VES, and E852 experiments, respectively [6, 7, 8]. .	11
1.6	The $J^P = 1^-$ nonet where the particles are grouped by charge on the horizontal axis, strangeness on the vertical axis, and isospin projection along the diagonal.	12
1.7	The $M(\eta\eta')$ from the BESIII collaboration. A Partial Wave Analysis was performed on the reaction $J/\psi \rightarrow \gamma\eta\eta'$ and an isoscalar resonance coined the $\eta_1(1855)$ with exotic quantum numbers was observed. This contribution is highlighted in dark purple [9]. .	13
2.1	An overview of the Jefferson Lab complex located in Newport News, Virginia. The CEBAF (located bottom left) provides the beam into the racetrack-shaped accelerator tunnel. Halls A, B, and C are located in the bottom right of the picture under the dome-like hills. Hall D is located at the top left of the picture which is where the GlueX experiment is located [10].	15
2.2	An overview of the Continuous Electron Beam Accelerator Facility (CEBAF). An electron beam is provided for the accelerator via the injector (in green). The beam then travels down one of the RF cavities and is steered by powerful magnets to keep the beam on the racetrack path. It makes up to 5.5 passes and is fed into one of the Halls A, B, C, or D [11].	16
2.3	An schematic diagram describing the injector that provides the electron beam to CEBAF. The photo-producing, bunching, and accelerating stages of the beam up until the beam is injected into the linear part of the accelerator are labelled [11]. . .	16
2.4	A picture of the RF linear accelerator portion of CEBAF. There are five beam pipes corresponding to the energy of the electrons. Lower energy electrons travel on the	

	top beam pipes while higher energy electrons travel in the beam pipes closer to the ground [10].	17
2.5	A diagram of the GlueX beamline is presented here. The electron beam enters into the hall from the left and interacts with the diamond radiator to produce a photon beam. The electrons are bent and their energies are tagged while the photon beam travels downstream through the collimator and reaches the Pair Spectrometer and Triplet Polarimeter used for measuring the flux and polarization, respectively [11]. . .	18
2.6	(a) Photon beam intensity versus energy as measured by the pair spectrometer (not corrected for instrumental acceptance). (b) Photon beam polarization as a function of beam energy, as measured by the triplet polarimeter, with data points offset horizontally by ± 0.015 GeV for clarity [12].	20
2.7	This is a diagram of the GlueX spectrometer. It consists of a superconducting solenoid magnet, the target, central drift chamber (CDC), forward drift chamber (FDC), barrel calorimeter (BCAL), forward calorimeter (FCAL), the start counter (SC), and time of flight (TOF) detectors [11].	21
2.8	A picture of the superconducting solenoid being installed in Hall D. This is used to bend charged particles that enter to determine their momentum [10].	21
2.9	A schematic for the start counter and target cell. The target for GlueX is LH_2 which is super-cooled in a pressurized vacuum chamber [11].	22
2.10	The drift chambers used in the GlueX experiment for charged particle tracking. On the left is the Central Drift Chamber (CDC) and on the right is the Forward Drift Chamber (FDC) [11].	23
2.11	The calorimeters used in the GlueX experiment for neutral particle reconstruction and timing information. On the left is the Barrel Calorimeter (BCAL) and on the right is the Forward Calorimeter (FCAL) [11].	25
2.12	The Time of Flight detector (TOF) used in the GlueX experiment for particle identification. The left photo was taken when the TOF was mounted and experiment ready. The right photo is taken from the TOF upgrade that took place in 2019 [11].	25
2.13	This is a diagram of the GlueX spectrometer with the Phase-II upgraded DIRC detector included. [11].	26
3.1	The beam energy distribution for generated Monte Carlo. The beam energy was generated for a range of 6.5 to 11.4 GeV. The coherent peak is maximal near an energy of 8.8 GeV.	27
3.2	This diagram shows particles p_1 and p_2 interacting to produce particles p_3 and p_4 . Imagine in this case for p_1 to be the photon beam, p_2 to be the target, p_3 is $\eta\eta'$ and p_4 is the recoil proton.	28
3.3	The Mandelstam variable $-t$ distribution, also referred as momentum transfer, for generated Monte Carlo. The slope generated for this process is $2.6 (\text{GeV}/c^2)^2$	28

3.4	The generated mass for the $\eta'\eta$ final state.	29
3.5	The normalized Momentum transfer $-t$ -distributions for accepted Monte Carlo (in red) and data (in blue). The data and MC are both using the entire run range for the 2018-08 run period.	29
3.6	The normalized mass distributions for the $\eta'\eta$ final state for accepted Monte Carlo (in red) and data (in blue). The data and MC are both using the entire run range for the 2018-08 run period.	30
4.1	The red line shows the value of the cut imposed on the FCAL shower quality factor. Events are kept to the right of this line, while the events to the left correspond to showers that are unlikely to come from photons and are thrown away.	33
4.2	The selected beam bunch lies between the red lines. The other beam bunches will be used later to subtract accidentals in the analysis. The two peaks nearest to the central peak are omitted to avoid leakage into the central peak.	34
4.3	The events lying in the range between the red lines for the target chamber are kept.	35
4.4	The red line shows the value of the cut imposed on the Confidence Level, which is a variable that relates how likely a combination is to come from the reaction of interest. Events to the right of the red line are kept which have a higher confidence of resulting from the reaction of interest.	36
4.5	An example of a combination pairing of two photons, $\gamma_1\gamma_3$, where a π^0 peak is clearly visible as directed by the red arrow.	37
4.6	Shown above are two-photon combination masses that contain π^0 contamination. The mass distributions are fitted with two Gaussian distributions added to a 1st order polynomial. The red distribution is signal plus background, the purple and blue distributions are the two Gaussian distributions, and the green distribution is the polynomial background. The magenta lines correspond to a 3σ range calculated from the fits.	38
4.7	Shown above are the two η candidates after applying a 3σ π^0 removal. These candidates are fit with two Gaussian distributions plus a 3rd order polynomial.	38
4.8	Plotted is the significance for the two η candidates as a function of π^0 removal from 1σ up to 5σ in increments of 0.5σ . The significance peaks at the π^0 removal range of 3σ	39
4.9	Missing Mass Squared distribution. The green lines indicate the removal of the tails outside of the range $(-0.04, 0.04)(GeV/c^2)^2$	40
4.10	Missing Mass Squared distribution in both data and signal Monte Carlo. The Monte Carlo distribution is normalized to the maximum number of entries in the data. The green lines indicate the removal of the tails outside of the range $(-0.04, 0.04)(GeV/c^2)^2$	41

4.11	Missing Energy distribution. The blue lines indicate the removal of the tails outside of a 3σ window.	42
4.12	Missing Energy distribution in both data and signal Monte Carlo. The Monte Carlo distribution is normalized to the the data. The green lines indicate the removal of the tails outside of a 3σ window.	42
4.13	Plotted is the two-dimensional distribution of the mass of the two η candidates. The colored boxes represent the list of selections applied which range from 1σ up to 4σ in increments of 0.5σ	43
4.14	Plotted is the $M(\eta\pi^+\pi^-)(GeV/c^2)$ after making a two-dimensional 1.5σ η selection. The distribution is fitted with Gaussian for the signal and a 3rd order polynomial for the background.	44
4.15	Plotted is the significance for the $M(\eta\pi^+\pi^-)$ as a function of a two η selection ranging from from 1σ up to 4σ in increments of 0.5σ . The significance peaks near 1.5σ and 2σ	44
4.16	The $M(\pi^+\pi^-)$ distribution is cut for events greater than $0.42 GeV/c^2$	45
4.17	The beam energy distribution is selected to be above $7.5 GeV$ since the analysis focuses on meson production near or above the coherent peak.	45
4.18	The Confidence Level which relates how likely a combination is to come from the reaction of interest. Events to the right of the green line are kept which have a higher confidence of resulting from the reaction of interest. Data is shown in blue, while signal Monte Carlo is presented in red.	46
4.19	Plotted is the $M(\eta\pi^+\pi^-)$ (GeV/c^2) after removing events with confidence level values less than 10^{-9} . The distribution is fitted with Gaussian for the signal and a 3rd order polynomial for the background.	47
4.20	Plotted is the significance for the $M(\eta\pi^+\pi^-)$ as a function of confidence level cut values ranging from 10^{-20} , 10^{-19} , ... 10^{-1} . The significance peaks near a value of 10^{-9} .	47
4.21	Selecting the η' for the reaction. There are two η s present, so there are two choices. .	48
4.22	By plotting the $M(\eta p)$ selecting the bachelor η , there is a clear N^* resonance corresponding to the N(1535) that is present in the data. Events to the left of the red line are removed.	49
4.23	After removing the N(1535) from the data, the $M(\eta'\eta)$ is plotted before and after the removal. The blue shaded region is before the removal and the green shaded region is after removal. Clearly, the N(1535) events are seen in the higher mass region of the $M(\eta'\eta)$. It is noted that there is 33% background estimated under the η'	50
4.24	Number of particles in an event at this stage of the analysis. The primary source of extra combinations comes from extra beam candidates	51

4.25	The accidentals are used for subtracting out-of-time photons that show up as in-time photons. The accidentals closest to the main peak are skipped to avoid over-subtracting events that lie within the tails of the in-time peak that bleed into these closest accidentals.	51
4.26	At this stage there is about 67% of the remaining $M(\eta\pi^+\pi^-)$ events that are signal considering a 2σ window using a Gaussian and polynomial background fit.	52
4.27	The $M(2\gamma)$ distributions have an estimated background of about 18% remaining under the η peak. This is used as a guide to understand how much background will be present in the constrained data set where the η masses are restricted to a δ peak at the η mass.	52
4.28	The final data selection criteria use to achieve an exclusive reaction of $\gamma p \rightarrow \eta'\eta p$	53
4.29	After matching the events that survive the kinematically fitted η s, the η' is fitted using the same methods previously. Using kinematically fitted η s clearly improves the resolution of the η' . This improves the signal percentage from 67% to 79%.	54
4.30	The final distribution $M(\eta\eta')$ after data selection. The mass distribution has an estimated 21% background remaining under the η'	54
5.1	The $M(\eta\eta')$ distribution split into bins of mass.	56
5.2	The yields for each $M(\eta\eta')$ bin are computed by fitting the $M(\eta\pi^+\pi^-)$ distribution with a Gaussian for the signal and a 3rd order polynomial for the background. The signal events are calculated using a 2σ window.	57
5.3	The Monte Carlo efficiencies as a function of $M(\eta'\eta)$. The efficiency is calculated by dividing the accepted MC over the generated MC. The efficiency for the 2017 run period is given in blue, the efficiency for the 2018-01 run period is given in red, and the efficiency for the 2018-08 run period is given in magenta.	59
5.4	The differential cross section in bins of $M(\eta'\eta)$. Statistical uncertainties are shown.	60
6.1	The differential cross section in bins of $M(\eta'\eta)$ for different η selections.	62
6.2	Plotted is Δ/σ_Δ , the significance for the Barlow test, in bins of $M(\eta'\eta)$ for different η selections.	62
6.3	The differential cross section in bins of $M(\eta'\eta)$ for different η' selections.	63
6.4	Plotted is Δ/σ_Δ , the significance for the Barlow test, in bins of $M(\eta'\eta)$ for different η' selections.	64
6.5	The differential cross section in bins of $M(\eta'\eta)$ for different $M(\eta p)$ selections.	64
6.6	Plotted is Δ/σ_Δ , the significance for the Barlow test, in bins of $M(\eta'\eta)$ for different $M(\eta p)$ selections.	65
6.7	The differential cross section in bins of $M(\eta'\eta)$. Statistical uncertainties are shown with the light green shaded blocks. The total uncertainty is the systematic uncertainty	

added in quadrature with the statistical uncertainty and is shown by the dark green error bars. 66

LIST OF ABBREVIATIONS

ATLAS	A Toroidal LHC (Large Hadron Collider) Apparatus
BCAL	Barrel Calorimeter
BEPCII	Beijing Electron-Positron Collider II
BESIII	Beijing Spectrometer III
CDC	Central Drift Chamber
CEBAF	Continuous Electron Beam Accelerator Facility
CERN	European Organization for Nuclear Research
CMS	Compact Muon Solenoid
COMPASS	Common Muon Proton Apparatus for Structure and Spectroscopy
cw	continuous wave
DIRC	Detection of Internally Reflected Cherenkov Light
doca	distance of closest approach
FCAL	Forward Calorimeter
FDC	Forward Drift Chamber
GlueX Experiment	Gluonic Excitation Experiment
Had-Spec	Hadronic Spectrum Collaboration
MC simulation	Monte Carlo simulation
ME	Missing Energy
MMS	Missing Mass Squared
PDG	Particle Data Group
pmt	photomultiplier tube
PS	Pair Spectrometer
PWA	Partial Wave Analysis
QCD	Quantum Chromodynamics
QED	Quantum Electrodynamics
rf	radio frequency
ST	Start Counter
srf	superconducting radio frequency
TAGH	tagger hodoscopr
TAGM	tagger microscope
TOF	Time-of-Flight
TPOL	Triplet Polarimeter

ABSTRACT

The GlueX experiment is located in Newport News, Virginia and aims to search for exotic quantum states that are not predicted by the quark model. These states include multi-quark configurations and configurations with excited gluons. This dissertation describes an investigation of the photo-production of $\eta\eta'$ which is expected to decay from an isoscalar partner to the $\pi_1(1600)$ with exotic quantum numbers $J^{PC} = 1^{-+}$. A detailed data selection study is presented to achieve an exclusive reaction $\gamma p \rightarrow \eta'\eta p$. A differential cross section in four bins of $M(\eta'\eta)$ is calculated. The cross section was calculated for a beam energy greater than 7.5 GeV. The mass bin from 1.7 to 2.1 GeV/ c^2 is the region where BESIII observed a candidate for the exotic η_1 . However, no significant features were observed in the cross section in this region to corroborate their observation. Nonetheless, there are some similarities such as the sharp rise near threshold and a peaking structure near 2 GeV/ c^2 . Systematic uncertainties are included in the calculation of the cross section using the Barlow test to consider the significance of certain data selections.

CHAPTER 1

INTRODUCTION

1.1 Brief History of Particle Physics

1.1.1 Electrons, Protons, and Neutrons: Classical Origins

It is hard to pinpoint when the field of particle physics was first formed, but there were substantial milestones achieved in the last century that helped shape what the field is today. J.J. Thomson's discovery of the electron in 1897 can be argued as the first major step towards the formation of particle physics [13]. Thomson observed that when cathode rays are emitted in the presence of a magnetic field, their rays are deflected. This suggested that the rays carry an electric charge and furthermore, the charge should be negative given the direction that the rays are deflected. Thus, it was hypothesized that maybe these rays are actually negatively charged particles. Thomson applied both an electric and magnetic field tuning their strength in such a way that when these rays interacted with the field, they would not deflect. From this, he was able to measure the velocity and charge-to-mass ratio of the negatively charged particles. It turned out the ratio was huge which can only be explained if the charge is really big or the mass is really small. Thomson coined the particles "corpuscles". These particles were later referred to as 'electrons' from the unit of charge that they carried named by George Johnstone Stoney [14],[1].

Thomson's model of the atom was the plum pudding model [15]. He believed that these negatively charged electrons are immersed in a positively charged "pudding". This view was disregarded once Ernest Rutherford performed his famous scattering experiment in 1909 [16]. The experiment showed that most of the mass of the atom as well as the positively charged particles are located at a central region (the "nucleus"). The experiment was performed by shooting a ray of alpha particles onto a thin sheet of gold. If the plum pudding model was correct, all of the alpha particles should be deflected by a small amount. However, it was observed that most of the alpha particles went through the gold foil. A few of them were deflected by large angles. Thus, Rutherford concluded that the alpha particles were hitting something hard, small, and heavy. The concentration of positive charge and most of the mass must be located near the center of the atom [1].

By 1914, a more sophisticated model of the atom was constructed by Niels Bohr [17], [18]. His model featured the electron orbiting the positively charged proton the same way as a planet orbits the sun. The electrical attraction works in this scenario the same way gravity works between planets and stars. By 1932, Chadwick had discovered the neutron [19], a neutral particle similar to the proton that also makes up the nucleus of an atom [1].

1.1.2 Photons

The early 1900s was a thriving time for discoveries in physics. New particles were being discovered and models of how the world describes interactions between these particles changed as new evidence surfaced from experiments. Near the time that the electron was discovered, Max Planck also found a new way to describe black-body radiation. He found it necessary to assume that black-body radiation is quantized with energies of the form

$$E = h\nu. \tag{1.1}$$

Here ν is the frequency of this quantized energy and h is what is known today as Planck's constant. This is where the first idea of quantized light or "photons" is introduced. Soon after, in 1905, Albert Einstein proposed the idea that quantization is a property of the electromagnetic field and used this idea to explain the photo-electric effect. If electromagnetic radiation is incident on a metal surface, it causes electrons to be emitted. The photon hits an electron and gives up energy $E = h\nu$ which is absorbed by the electron causing the electron to break away from the surface of the metal as long as $h\nu > W$ where W is called the work function of the metal [20]. A.H. Compton's 1923 experiment [21] showed that light scattered off of a stationary particle is shifted in wavelength by

$$\lambda' = \lambda + \lambda_c(1 - \cos(\theta)). \tag{1.2}$$

Here λ is the incident wavelength, θ is the scattering angle, λ' is the scattered wavelength, and λ_c is the Compton wavelength given by

$$\lambda_c = h/mc. \tag{1.3}$$

Thus, light behaves as a particle. Gilbert Lewis coined the term "photon" to describe a quanta of light [1].

1.1.3 Mesons

A big question of the early 20th century was: how is the nucleus bound together? Protons should be repelling one another since they have the same charge. Since they clump together to form nuclei there must exist a force with a strength greater than the electromagnetic force. Thus, the term “strong force” was coined for this phenomena. However, since humans do not experience this force every day like they do the electromagnetic force, this strong interaction must be very short range. In 1934, Yukawa made the first significant theory of the strong force [22]. He hypothesized that there must be a field that binds protons and neutrons together similar to the electric field that exists for electrons and protons. Furthermore, this field must be quantized and can be described by the mediation of a particle. The mediator particle should be about 300 times more massive than the electron and one sixth the mass of the proton. The term “meson” or “middle-weight” was coined for this mediator particle. Similarly “lepton” or “light-weight” was used for electrons and “baryon” or “heavy-weight” was used for protons and neutrons [1].

In 1947, pions and muons were discovered to make up cosmic rays interacting with nuclei [23]. The pion turned out to be the Yukawa meson that was proposed to mediate the strong force. It wasn't until about thirty years later once heavier mesons were discovered that the mediator of the strong force was no longer considered Yukawa's pion. In fact, the strong force operates at a much smaller scale. Protons and neutrons are composite particles composed of quarks [24], [25]. These quarks are bound together by the strong force mediator particle: the gluon. Near the later part of the 20th century, the Standard Model of Particle Physics was established as the best description of most of the phenomena we observe on the microscopic scale [1].

1.2 Modern Particle Physics

1.2.1 The Standard Model

All of the observable matter in the universe is made up of quarks and leptons. These particles interact through forces governed by the exchange of different gauge particles. The Standard Model of particle physics is a model that describes the interactions between these various particles. There are three generations of leptons: the electron, muon, and tau. Each of these has a corresponding neutrino: the electron-neutrino, muon-neutrino, and tau-neutrino. These particles have charge, electron number, muon number, and tau number. There are six anti-leptons that have opposite

values for these numbers. In total there are 12 leptons. The leptons with their corresponding quantum numbers are given in Table 1.1.

Table 1.1: Lepton generations with their corresponding charge, electron, muon, and tau numbers [1]

Leptons & Antileptons	Charge	Electron Number	Muon Number	Tau Number
e^-	-1	1	0	0
ν_e	0	1	0	0
μ	-1	0	1	0
ν_μ	0	0	1	0
τ	-1	0	0	1
ν_τ	0	0	0	1

Quarks come in six flavors: up, down, strange, charm, top, and bottom. Each quark can come in three different colors: red, green, or blue. They have corresponding anti-quarks that come in three different anti-colors: anti-red, anti-green, or anti-blue. In total, there are 36 different types of quarks. The quarks with their corresponding quantum numbers are given below in Table 1.2.

Table 1.2: Classification of quarks with their corresponding charge, downness, upness, strangeness, charm, beauty, and top numbers [1]

Quarks	Charge	Down	Up	Strange	Charm	Beauty	Top
d	-1/3	-1	0	0	0	0	0
u	2/3	0	1	0	0	0	0
s	-1/3	0	0	-1	0	0	0
c	2/3	0	0	0	1	0	0
b	-1/3	0	0	0	0	-1	0
t	2/3	0	0	0	0	0	1

Finally, we have the gauge bosons. These particles are mediators for the fundamental forces. The photon mediates the electromagnetic force and is sometimes denoted by γ . The W^\pm, Z^0 bosons are mediators for the weak force. The strong force is mediated by 8 gluons sometimes denoted by g . Theoretically, gravity should be mediated by a particle called the graviton. However, the Standard Model does not include gravity. The Higgs boson is responsible for the mass of all known particles and was discovered in 2012 by the ATLAS and CMS collaborations at CERN [26]. A picture including all of the particles in the Standard Model is given collectively in Fig. 1.1.

Standard Model of Elementary Particles

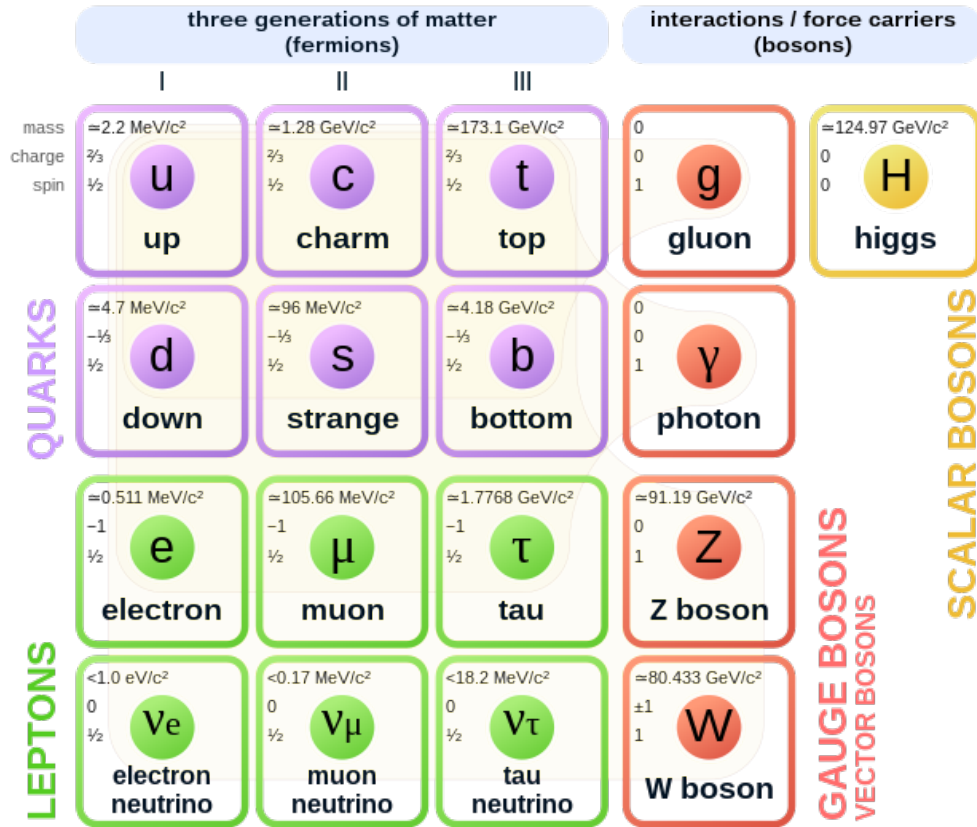


Figure 1.1: This diagram illustrates the standard model of particle physics. Quarks are represented with purple, leptons are represented with green, and gauge bosons are in orange and yellow [2].

1.2.2 Quantum Chromodynamics (QCD)

Quarks interact via the strong force through the gluon mediators and form color-neutral hadrons. These hadrons are classified in two ways: as bound states of three quarks called baryons, or as quark and anti-quark bound state pairs called mesons. The prototypical example of hadrons include the nucleons (neutrons and protons) which are found in the nucleus of atoms. Quantum Chromodynamics (QCD) is the theory within the Standard Model that describes the interaction between quarks and gluons. QCD is inspired by an analogous theory called Quantum Electrodynamics, or (QED). QED describes how electrically charged particles interact by exchanging photons. Photons do not interact with one another because they don't carry electric charge. The analogous construct

in QCD is called color charge. While there is only one type of electric charge in QED, QCD color charge comes in three different forms as described earlier. Just as electric charge interacts by exchanging photons in QED, color charge interacts by exchanging gluons in QCD. Unlike the photon that does not carry electric charge, gluons do carry color charge and can interact with one another.

The strength of QCD interactions at different energy scales gives rise to asymptotic freedom and color confinement. If there is a high momentum transfer Q and the distance between quarks is small, the strength of the interaction is diminished in a process called asymptotic freedom. The value of Q is inversely proportional to the distance between the quarks. Thus, the strength of the interaction actually decreases as the distance between the quarks decreases (Q increases). The interaction strength is described by a coupling parameter α_s and depends on the momentum transfer as shown in Fig. 1.2. For high Q values, α_s approaches zero.

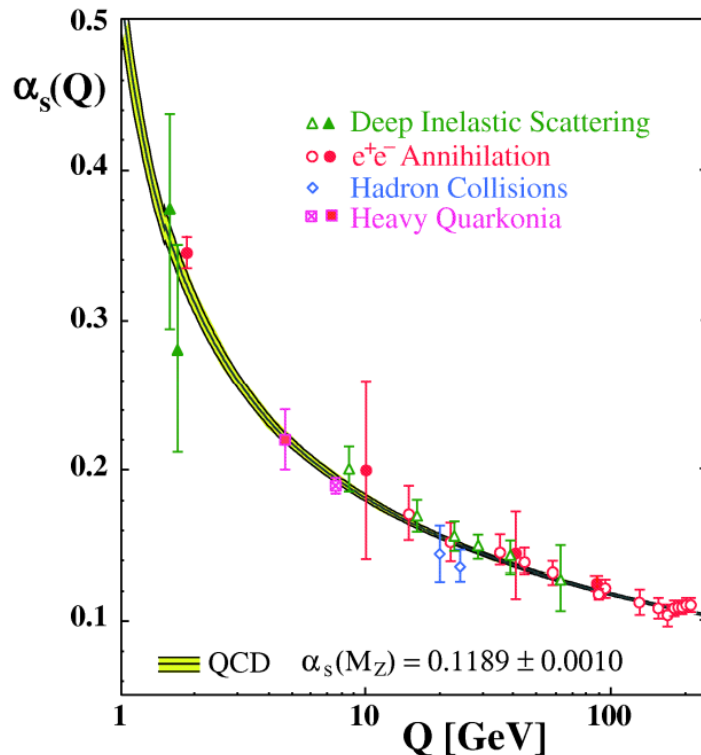


Figure 1.2: The coupling constant $\alpha_s(Q)$ as a function of the momentum transfer Q . Theoretical predictions are given by the line and the points give the experimental results. Reproduced from [3].

If there is a low momentum transfer and the distance between the quarks is large, then confinement dominates. Confinement is the idea that quarks and gluons are permanently bound together

in colorless states. Since mesons can be modeled as bound states of a quark-antiquark pair, they carry color and anticolor charges and are, therefore, colorless. They are bosons that have integer spin. Baryons can be modeled as three-quark systems that are color neutral. They are fermions with half-integer spin. Since hadrons have to be colorless, quarks cannot exist on their own. Plucking a quark from a hadron requires an energy greater than that needed to produce a quark-antiquark pair so quarks never roam free in the wild.

1.3 The Classical Quark Model

1.3.1 Symmetries

Hadronic physics studies the relationship between quarks and the strong force at an energy scale on the order of 10 GeV. Mesons and baryons are grouped together by symmetry properties such as their mass, charge, spin and isospin. Consider a proton and a neutron which have similar masses (within a percent or so) and are distinguished by their electric charge. A proton is positively charged while a neutron is neutral. Ignoring the electromagnetic force, the proton and neutron would be grouped under a single category: the nucleon. Similarly, the three pions: π^+ , π^0 , π^- would become the pion. The strong force has a degeneracy that is only lifted when we consider electromagnetic interactions. These degenerate eigenstates are a consequence of the underlying symmetry of the QCD Lagrangian. The Lagrangian has an SU(2) symmetry called isospin symmetry. Introducing electromagnetic interactions breaks this symmetry and multiplets are formed. The first example of an SU(2) multiplet is the (fundamental) two-dimensional representation which corresponds to two states up or down (u, d). Another example would be the proton (that has $I_3 = +\frac{1}{2}$) and the neutron (that has $I_3 = -\frac{1}{2}$). Higher dimensional representations also exist. The (regular) three-dimensional representation corresponds to three states; for example the three pions: π^+ , π^0 , π^- . The four-dimensional representation corresponds to four states; for example the four delta particles: Δ^{++} , Δ^+ , Δ^0 , Δ^- [27]. It should be noted that these symmetries are approximate unlike, for example, the SU(3) color symmetry of the Standard Model, which is exact.

1.3.2 Selection Rules

Group structures are created by collecting particles that have the same spin and parity, i.e. particles that share the same J^P or J^{PC} quantum numbers. Here J is the total angular momentum that ranges from $|l - s| \leq J \leq |l + s|$. P is the parity that is given by $P = (-1)^{l+1}$ and C is the charge conjugation given by $C = (-1)^{l+s}$. The analysis described in this dissertation focuses

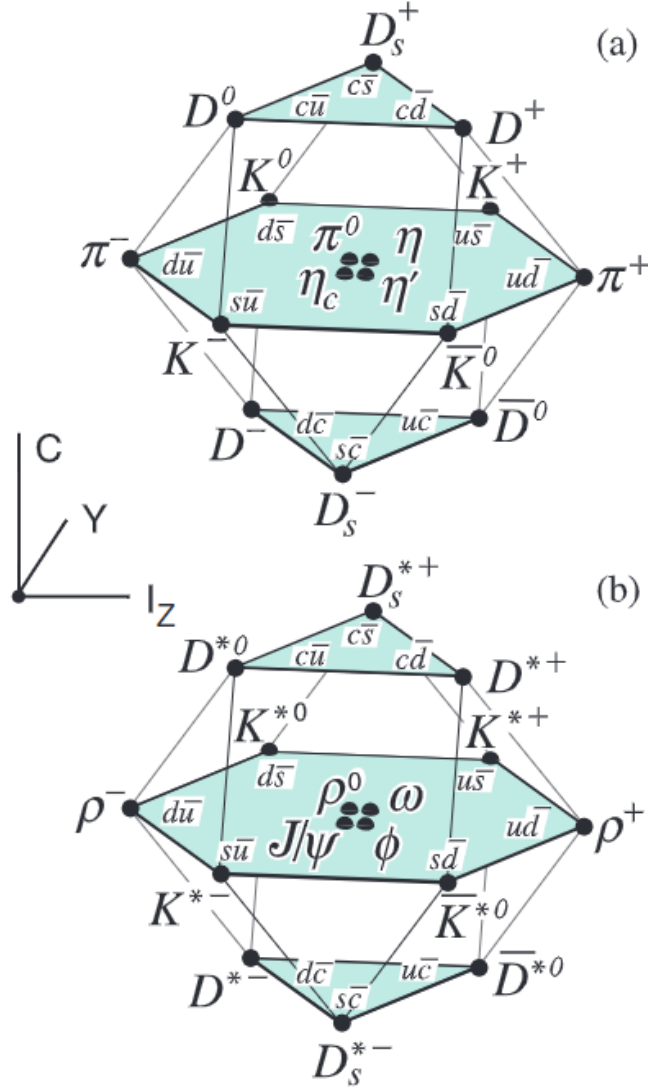


Figure 1.3: Given here are the SU(4) weight diagrams for the $l = 0$ pseudoscalar meson (a) and vector meson (b) multiplet. The nonet structures are the highlighted planes in the center of the 16-plet. They are arranged based on strangeness, charge, and isospin [4]

on meson production, so the examples given are related to mesons. Figure Fig. 1.3 shows the $l = 0$ pseudoscalar meson multiplet with $J^{PC} = 0^{-+}$ (a) and the vector meson multiplet with $J^{PC} = 1^{--}$ (b). There are highlighted planes in the center of the 16-plet structures that are the nonet structures. The nonets are grouped according to the particle's I_3 component of isospin, strangeness, and charge. The I_3 component of isospin changes for the particles as you move along the horizontal axis from the ρ^- to the ρ^+ . Moving along the vertical axis from the K^{*-} , K^{*0} to the

K^{*0}, K^{*+} changes the strangeness, and moving along the diagonal axis changes the charge [4]. As elegant as this description of hadron classification is, this is not the full picture. The next section will introduce some of the classifications that are outside of this quark model picture.

1.4 Exotic & Hybrid Mesons

The classical quark model allows for $q\bar{q}$ and qqq states. However, the QCD Lagrangian can allow for states of pure glue, multiquark states like tetraquarks or pentaquarks, and states that have gluons in their valence band. For the GlueX experiment, the search for hybrid mesons is the main focus. Hybrid mesons are similar to mesons in that they are composed of a quark-antiquark pair. However, they also contain excited gluons in their valence shell. This extra gluonic excitation can give rise to a richer spectrum of quantum numbers than are allowed in the classical quark model. Hybrid mesons that have quantum numbers that are not allowed by the classical quark model are called exotic mesons.

Perturbative QCD is useful when the strong force coupling constant α_s is small at short quark distances or at high enough energies. For the energies that will be presented in this analysis, QCD is not perturbative so a non-perturbative approach is necessary. One of the leading theories is Lattice QCD that uses a finite grid to represent space-time instead of assuming a continuum. The number of degrees of freedom is reduced from infinite to something finite (which depends on the lattice spacing used) so that theory can be calculated on powerful computers [5]. The Hadron Spectrum Collaboration (Had-Spec) used Lattice QCD for mapping a spectrum of predicted isoscalar and isovector meson states. They used a $391 \text{ MeV}/c^2$ pion mass in their calculations which is much heavier than the measured pion mass. The exact scale of their predictions is not expected to agree with experiment, but the relative positions should agree. A plot for the spectrum is given below where the $I = 1$ isovector states are given in blue, the $I = 0$ isoscalar states are black and green corresponding to light quark content (up or down) and strange quark content, respectively. Gluonic excitations are given in orange. The lightest exotic meson is expected to have quantum numbers $J^{PC} = 1^{-+}$ (See Fig. 1.4). This leads to the main motivation behind the analysis undertaken in this work.

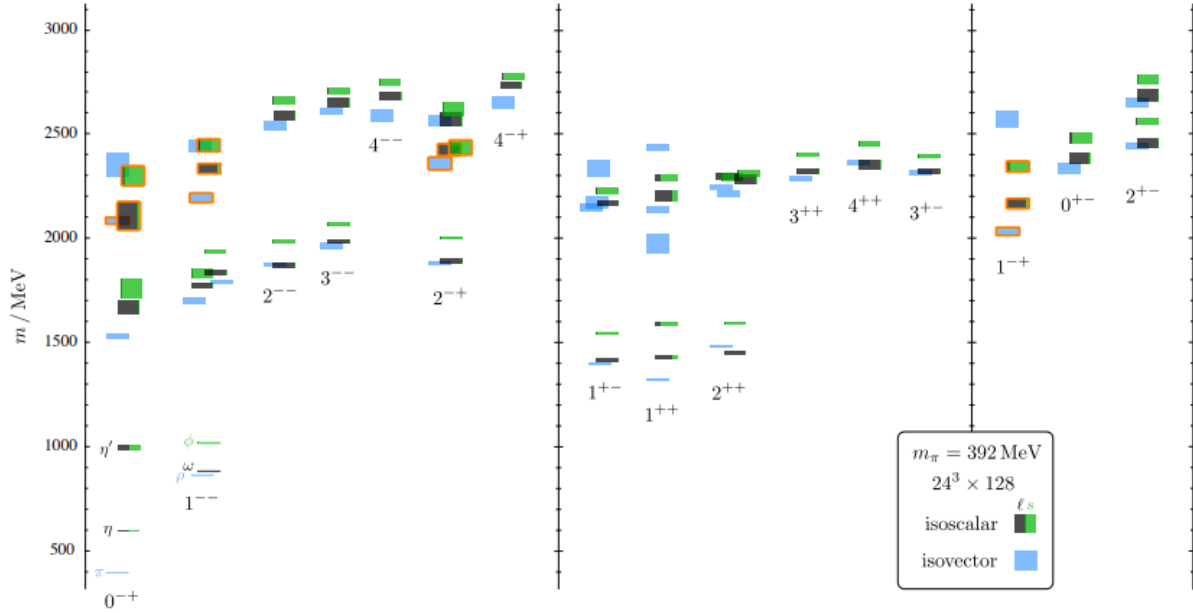


Figure 1.4: Lattice QCD predictions for isoscalar (green and black) and isovector (blue) mesons. Vertical height of each box gives statistical uncertainty of the mass. States outlined in orange are the lowest-lying states having dominant overlap with operators featuring a chromomagnetic construction. Source: Fig. 11 of Ref. [5]

1.5 Motivation

The main goal of the GlueX experiment is to search for hybrid mesons. All meson states carry J^{PC} quantum numbers. Hybrid mesons can include states with allowed quantum numbers as well as exotic states that carry quantum numbers that are not allowed by the quark model. The quark model allows states including $J^{PC} = 0^{-+}, 0^{++}, 1^{--}, 1^{+-}, 1^{++}$, etc. However, QCD also allows for states such as $J^{PC} = 0^{--}, 0^{+-}, 1^{-+}$, etc. Distinction between conventional states and hybrid states with non-exotic quantum numbers is important. This is because it is possible for hybrid states with non-exotic quantum numbers to mix with conventional states. Meson resonances up to 2 GeV are only moderately modeled so far and there is not much data on resonances above 2.2 GeV for any light quark sector [28]. Therefore, the analysis of $\eta\eta'$ is important since this state is expected to decay from a hybrid candidate.

1.5.1 The $\pi_1(1600)$

One of the most studied exotic hybrid candidates is the $\pi_1(1600)$. An earlier experiment regarding this hybrid was the E852 experiment at Brookhaven National Laboratory. This experiment used a pion beam at 18 GeV to analyze the reaction $\pi^- p \rightarrow \eta' \pi^- p$. An amplitude analysis and partial wave decomposition was performed. The $\eta' \pi^-$ state was decomposed into three partial waves: $J^{PC} = 1^{-+}, 2^{++}$, and 4^{++} . The exotic 1^{-+} partial wave dominated this decomposition with a mass of $1.597 \pm 0.010^{+0.045}_{-0.010} \text{ GeV}/c^2$ which corresponds to the exotic $\pi_1(1600)$ [29]. Similarly, the VES collaboration at the Institute for High Energy Physics (Protvino) used a pion beam at 28 GeV and performed a Partial Wave Analysis (PWA) on the same reaction [7]. More recently, the COMPASS collaboration at CERN used a 191 GeV pion beam to study the same reaction and also performed a PWA [6]. Plots from each of these experiments are give in Fig. 1.5.

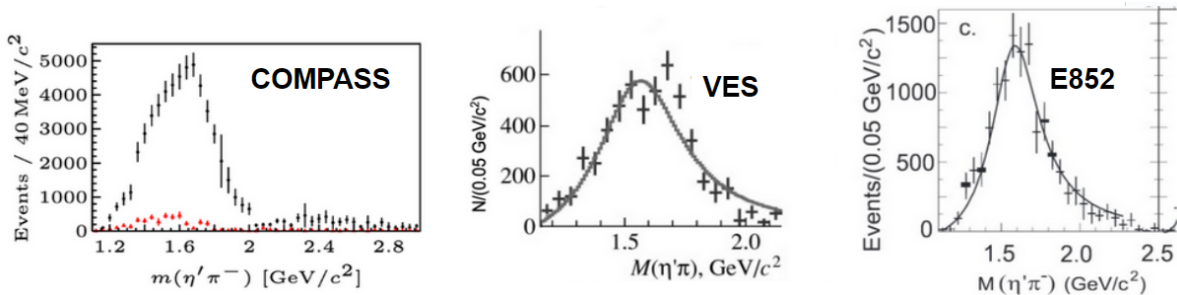


Figure 1.5: The $M(\eta' \pi)$ from the COMPASS, VES, and E852 experiments, respectively [6, 7, 8].

1.5.2 The Hypothesized η_1

The reason that the $\pi_1(1600)$ is important for the $\eta \eta'$ channel has to do with the grouping of hadrons that was mentioned earlier. It is expected that the $\pi_1(1600)$ belongs to a nonet with exotic quantum numbers $J^{PC} = 1^{-+}$. In fact, lattice calculations predict there are two nonets corresponding to $J^{PC} = 1^{-+}$. One of these nonets includes the η_1 and η'_1 which are isoscalar partners to the $\pi_1(1600)$. Shown here is the nonet structure for the $J^P = 1^-$ nonet that includes these isoscalars Fig. 1.6. The quantum numbers of both the η_1 and η'_1 allow for the decay into $\eta \eta'$ which makes this the primary motivation for studying this channel.

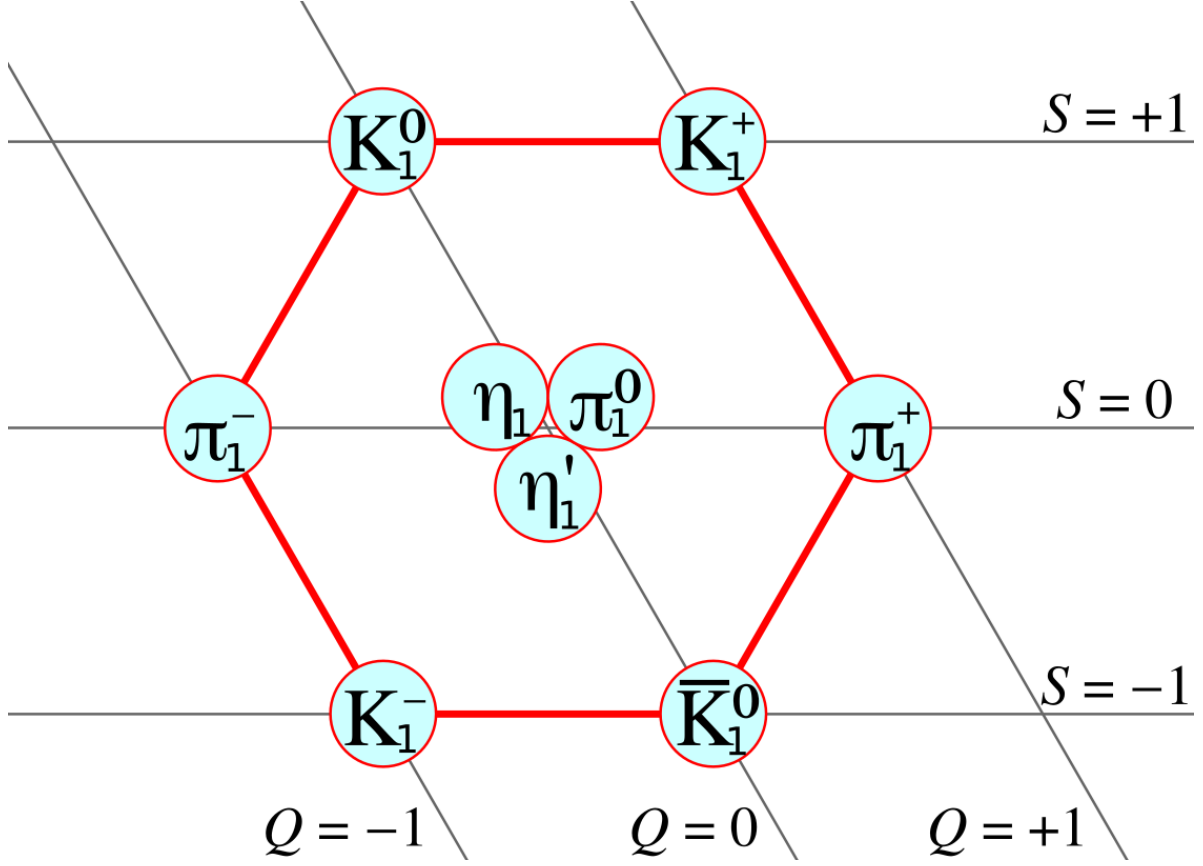


Figure 1.6: The $J^P = 1^-$ nonet where the particles are grouped by charge on the horizontal axis, strangeness on the vertical axis, and isospin projection along the diagonal.

1.5.3 The $\eta_1(1855)$ at BES III

An important study for this channel was the PWA of $J/\psi \rightarrow \gamma\eta\eta'$ with the BESIII detector operating at the BEPCII storage ring. A sample of $(10.09 \pm 0.04) \times 10^9 J/\psi$ events was collected from the experiment operating at a center-of-mass energy of 3.89 GeV and peak luminosity of $1 \times 10^{33} \text{ cm}^{-2} \text{ s}^{-1}$. For the decay $\eta' \rightarrow \eta\pi^+\pi^-$ where $\eta \rightarrow \gamma\gamma$, the experiment measured $\sim 4,800$ events and measured $\sim 10,500$ events for $\eta' \rightarrow \gamma\pi^+\pi^-$. They claim to have made the first observation of an exotic isoscalar state with quantum numbers $J^{PC} = 1^{-+}$ labelled the $\eta_1(1855)$ that has measured mass and width of $1855 \pm 9_{-1}^{+6} \text{ MeV}/c^2$ [9]. The $M(\eta\eta')$ is given with its various partial wave decompositions in the figure below Fig. 1.7.

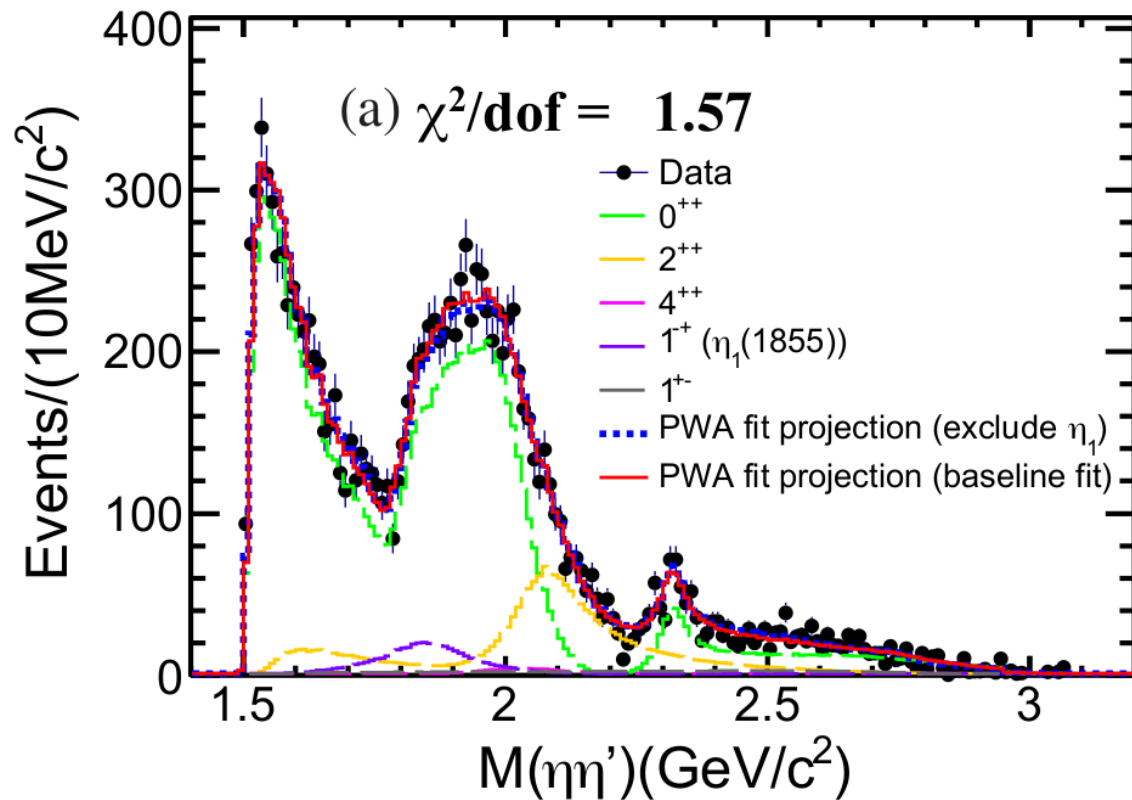


Figure 1.7: The $M(\eta\eta')$ from the BESIII collaboration. A Partial Wave Analysis was performed on the reaction $J/\psi \rightarrow \gamma\eta\eta'$ and an isoscalar resonance coined the $\eta_1(1855)$ with exotic quantum numbers was observed. This contribution is highlighted in dark purple [9].

CHAPTER 2

THE GLUEX EXPERIMENT

2.1 Overview of Jefferson Lab

The Gluonic Excitation experiment (GlueX experiment) is located at Thomas Jefferson National Laboratory in Newport News, Virginia. The Continuous Electron Beam Accelerator Facility (CEBAF) (or Continuous Electron Beam Accelerator Facility) provides an electron beam that is directed to Halls A, B, C, and D. Halls A, B, C were recently upgraded with a maximum beam energy of 11.5 GeV, and Hall D was created for the GlueX experiment with a maximum beam energy of 12 GeV. The CEBAF is composed of a polarized electron source with an injector and a pair of superconducting RF linear accelerators that are connected by two arcs with steering magnets. The beam makes up to 5.5 successive orbits and is directed into one of the four halls.

2.2 CEBAF

The CEBAF produces an electron beam by the use of laser light interacting with a gallium-arsenide wafer. CEBAF uses superconducting radiofrequency (SRF) technology and is the first large-scale application of this technology in the world. Its purpose is to probe the quark structure of the nucleus [8]. This facility produces continuous wave (cw) operations, can achieve currents of $200 \mu A$, and can distribute beam into multiple halls at once. The laser light causes electrons that are bound to the wafer to leave the surface. The electrons are then forced by magnets to become a stream of particles. The accelerator has a racetrack shape. There are two linear accelerator regions and two arc regions. The electron beam travels into the linear region first. The linear Radio Frequency (RF) cavities boost the energy of the beam. These superconducting cavities are cooled to a temperature near 2 Kelvin. The beam then arrives at an arc region where the electron beam interacts with magnets that steer and focus the beam. The total length of the racetrack is $7/8$ of a mile and the tunnel is located 25 feet beneath the ground surface [30].

2.2.1 Injector

The CEBAF injector is what provides the electron beam to the accelerator. The beam is created using a photo cathode gun as shown in the diagram Fig. 2.3. There is a pre-buncher cavity



Figure 2.1: An overview of the Jefferson Lab complex located in Newport News, Virginia. The CEBAF (located bottom left) provides the beam into the racetrack-shaped accelerator tunnel. Halls A, B, and C are located in the bottom right of the picture under the dome-like hills. Hall D is located at the top left of the picture which is where the GlueX experiment is located [10].

after the cathode guns that bunches the beam for the first time. After the pre-buncher, the beam reaches apertures that limit how much is emitted A_1 and A_2 and then reaches a chopper. The beam chopper regulates the timing and longitudinal component of the beam. Beams that are outside of the chopper radius will not pass through to the next stage. The next stage is the second or main

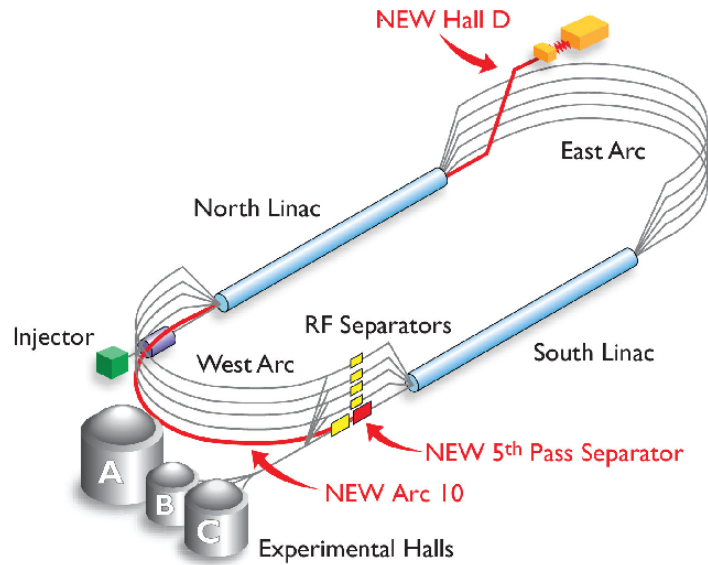


Figure 2.2: An overview of the Continuous Electron Beam Accelerator Facility (CEBAF). An electron beam is provided for the accelerator via the injector (in green). The beam then travels down one of the RF cavities and is steered by powerful magnets to keep the beam on the racetrack path. It makes up to 5.5 passes and is fed into one of the Halls A, B, C, or D [11].

bunching of the beam. Following this is the capture stage. These are crucial for the energy spread of the beam. The bunch length cavity then tunes the beam and measures its timing. The beam bunches are accelerated by superconducting radio frequency (SRF) cavities and are steered and focused by magnets. Faraday cups are used to determine the current of the beam [31].

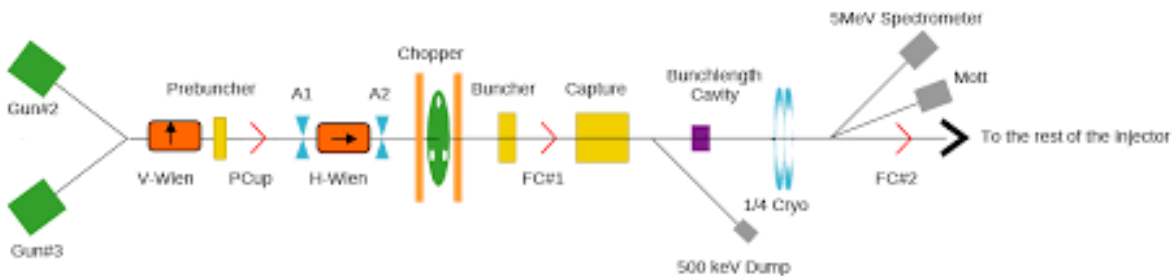


Figure 2.3: An schematic diagram describing the injector that provides the electron beam to CEBAF. The photo-producing, bunching, and accelerating stages of the beam up until the beam is injected into the linear part of the accelerator are labelled [11].

2.2.2 RF Linear Accelerators and Linac

The beam bunches leave the injector to be accelerated in linear RF cavities that are super-cooled using liquid Helium. Standing RF electromagnetic waves in phase with the bunches are responsible for boosting the momentum of the beam bunches. As the bunches enter, there are collections of negative and positive charges that push the bunches forward. The beam bunches arrive at the arc section of the accelerator and are steered using magnets so that they turn 180 degrees and get again boosted by another linear section by the process just described. One of the magnets separates the beam bunches based on their energies. The less energetic bunches are bent upward to the higher beam pipes. Once the beam bunches have passed five successive orbits, they can be fed into Hall D [32].



Figure 2.4: A picture of the RF linear accelerator portion of CEBAF. There are five beam pipes corresponding to the energy of the electrons. Lower energy electrons travel on the top beam pipes while higher energy electrons travel in the beam pipes closer to the ground [10].

2.3 Photon Beam

2.3.1 Diamond Radiator

Once the electron beam has entered Hall D, it hits a diamond crystal radiator with a thickness of $50 \mu\text{m}$. As the electrons interact with the lattice structure of the crystal, the electrons produce

coherent bremsstrahlung radiation. The diamond radiator has four different possible orientations: 0 degrees (parallel to the lab floor), 45 degrees, 90 degrees (perpendicular to the lab floor), and 135 degrees. 150 nA current is incident on the amorphous radiator while 100 nA is incident on the diamond radiator. Different currents for the radiators are used in order to get similar amount of statistics. Between different runs, the radiator is changed to different orientations. An amorphous radiator is also used for reference that provides an unpolarized beam [32].

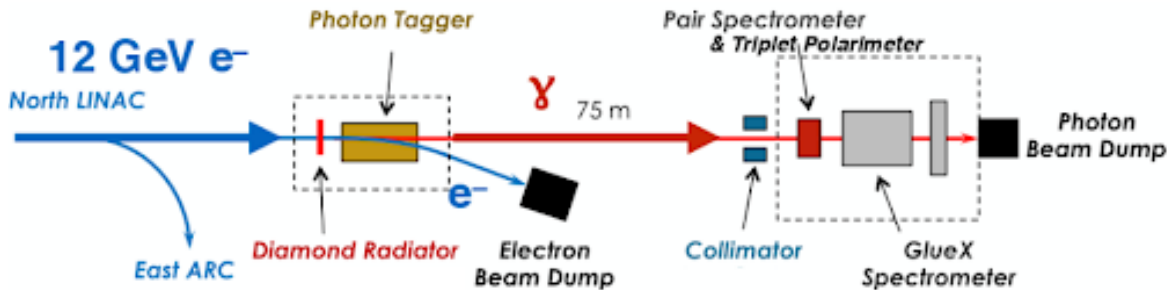


Figure 2.5: A diagram of the GlueX beamline is presented here. The electron beam enters into the hall from the left and interacts with the diamond radiator to produce a photon beam. The electrons are bent and their energies are tagged while the photon beam travels downstream through the collimator and reaches the Pair Spectrometer and Triplet Polarimeter used for measuring the flux and polarization, respectively [11].

2.3.2 Photon Tagging

A tagger magnet redirects the electrons based on their energy, whereas electrons that don't lose a certain amount of energy after passing through the radiator go into a beam dump. The tagger microscope (TAGM) and the tagger hodoscope (TAGH) detect the electrons that lie within the coherent peak region and outside the coherent peak region, respectively. In order to do this, the TAGM must have a higher resolution than the TAGH since the coherent peak region is only a fraction of the beam energy spread. The photons then travel 75 m to a collimator made of a lead block which has 3.4 mm and 5.0 mm openings. Since the angular distribution of the coherent photons is less than the spread of the incoherent photons, the collimator reduces the amount of incoherent photons entering the hall [32].

2.3.3 Triplet Polarimeter

After passing through the collimator, the beam then reaches the triplet polarimeter (TPOL) which is located between the collimator and the pair spectrometer (PS). The beam interacts on a

beryllium foil to create triplet photoproduction where the $e^+ e^-$ pair is detected in the PS and the recoil e^- is detected by the TPOL. From the recoil e^- , the angular distribution is measured to find information on the photon polarization using the relation

$$\sigma = \sigma_0[1 - P_\gamma \Sigma \cos(2\phi)]. \quad (2.1)$$

Here σ is the polarized cross section, σ_0 is the unpolarized cross section, P_γ is the degree of polarization for the beam photon, Σ is the beam asymmetry, and the azimuthal angle of the recoil electron is ϕ . By fitting the measured azimuthal angle of the electron, the degree of polarization can be extracted where the polarized and unpolarized cross sections as well as the beam asymmetry are calculated using QED [33], [34].

2.3.4 Pair Spectrometer

The beam then passes through the Pair Spectrometer (PS) which measures the flux. A foil converter pair produces $e^+ e^-$ pairs that are separated by a dipole magnet and detected by a hodoscope that measures energy and timing. The energy range that can be determined corresponds to a photon energy between 6 and 12 GeV . Knowing the beam flux from the TPOL can aid in calibration of the photon tagger [35].

2.4 GlueX Spectrometer

After the photon beam is produced from coherent bremsstrahlung radiation and information on the flux and polarization of the beam has been collected, the beam reaches the spectrometer. The GlueX spectrometer is a nearly 4π hermetic detector. It consists of a superconducting magnet to measure charged particle's momentum, drift chambers for charged particle tracking, electromagnetic calorimeters for reconstruction of neutral particles, a start counter to measure the time of the photon-proton interaction, and a time-of-flight detector to determine particle identification Fig. 2.7.

2.4.1 Solenoid

Surrounding the apparatus is a superconducting magnet. At a nominal current of 1350 A, the magnet has a field strength of 2 T. It has a diameter of 2 m and is 4.8 m in length. There are four superconducting coils and cryostats that are super-cooled using liquid helium. As charged particles enter the magnetic field, their trajectory will change due to the magnetic field. The particles have a radius of curvature directly relating to their momentum [36].

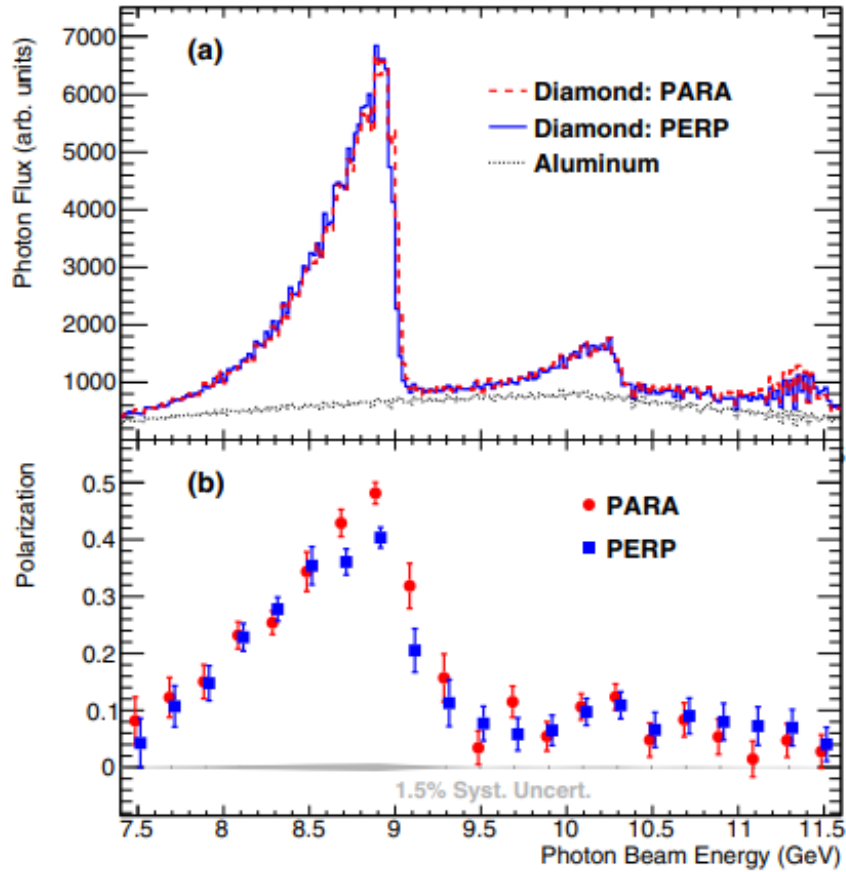


Figure 2.6: (a) Photon beam intensity versus energy as measured by the pair spectrometer (not corrected for instrumental acceptance). (b) Photon beam polarization as a function of beam energy, as measured by the triplet polarimeter, with data points offset horizontally by ± 0.015 GeV for clarity [12].

2.4.2 Target and Start Counter

The target is composed of a pulse tube cryo-cooler, condenser, and the target cell. The target used for the GlueX experiment is LH_2 , liquid hydrogen which is encased in a vacuum chamber made from aluminum and stainless steel. It is cooled to a temperature of 20.1 K which is 1 K higher than the operating temperature. It is also pressurized to 19 Psia. Measuring along the z -axis and defining the start of the solenoid as the zero point, the target begins at 50 cm and extends 30 cm [37]. The start counter (ST) is located outside of the target cell. It measures the time of the proton-photon beam interaction. The photon beam is sent in bunches of 4 ns and therefore the ST gives information on which beam bunch hits the target at a given time. It is shaped with a conical

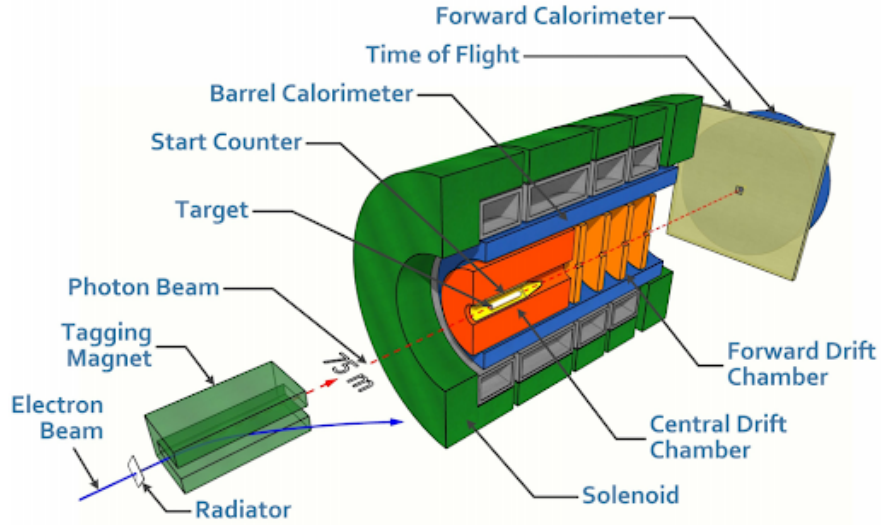


Figure 2.7: This is a diagram of the GlueX spectrometer. It consists of a superconducting solenoid magnet, the target, central drift chamber (CDC), forward drift chamber (FDC), barrel calorimeter (BCAL), forward calorimeter (FCAL), the start counter (SC), and time of flight (TOF) detectors [11].



Figure 2.8: A picture of the superconducting solenoid being installed in Hall D. This is used to bend charged particles that enter to determine their momentum [10].

end connected to a cylindrical body that is made up of 30 scintillator paddles. The ST can resolve beam photons with an intensity up to $10^8 \gamma/s$ [38].

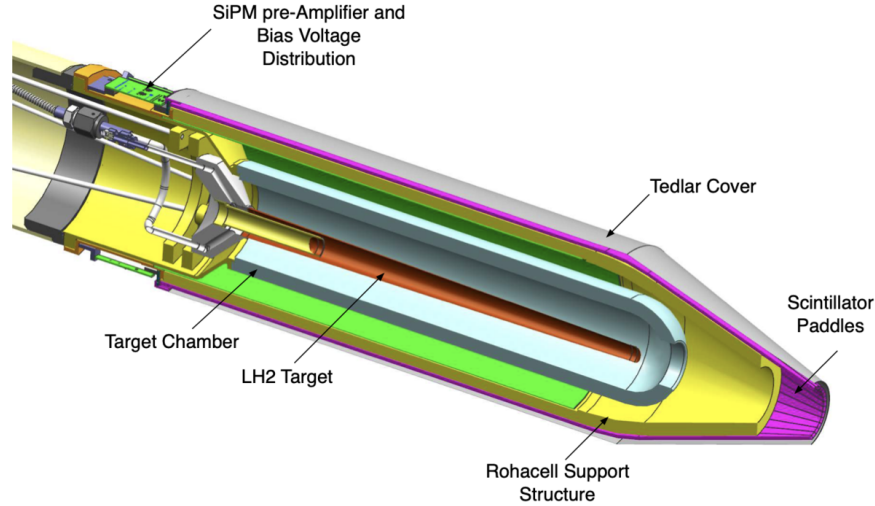


Figure 2.9: A schematic for the start counter and target cell. The target for GlueX is LH_2 which is super-cooled in a pressurized vacuum chamber [11].

2.4.3 Charged Particle Tracking

There are two drift chambers, the Central Drift Chamber (CDC) and the Forward Drift Chamber (FDC) Fig. 2.10. These are responsible for charged particle tracking. They provide information for a particle's position, timing, and energy deposition. Both of the drift chambers are filled with a mixture of argon and carbon dioxide gas. Charged particles enter the chambers and ionize this gas. When charged particles enter the magnetic field they bend. How much they bend, or the radius of curvature, is directly related to the particle's momentum. The drift chambers are able to reconstruct a particle's "track". A particle's "track" is a term used to describe its measured trajectory and momentum.

Central Drift Chamber. The CDC helps with tracking a particle using straw tubes with sense wires inside them at a high voltage. The tubes are filled with mixture of 50% argon and 50% CO_2 gases. This gas will ionize when charged particles enter the wires, creating free electrons that leave behind positively charged ions. The drift velocity of these electrons is well-defined when an external electric field is present. The straws provide the electric field due to each having a thin anode wire located at the center. The straws carry an applied voltage of +2125 V with respect to the surrounding tube. They are 1.5 m in length with a diameter of 1.575 cm. Electrons are collected by the anode wires and their drift time is measured. The distance of closest approach (DOCA) can be determined. This is done for all the straws in the CDC to determine the most accurate estimate

for the momentum and trajectory of a particle. The CDC is capable of detecting charged particles within a range of $6^\circ < \theta < 168^\circ$ with an optimal range of $29^\circ < \theta < 132^\circ$. Here θ is the polar angle of the electron's trajectory. The CDC has a spatial resolution of $200 \mu\text{m}$. Information on tracking the path of charged particles, timing, and the energy deposited as a function of distance can be gathered from the CDC. For particles with smaller angles, the FDC is used [39], [40], [41].

Forward Drift Chamber. The FDC is located downstream of the CDC and measures forward travelling particles. Using 24 cells with wire and cathode readouts, the FDC tracks particles and measures energy deposited as a function of distance for forward going particles. It is filled with a mixture of 40% argon and 60% CO_2 gases. The cells have sets of anode wires set at a voltage of +2200 V as well as field wires set at a negative voltage of -500 V that are located between the anode wires to enhance the electric field. The transverse distance of a track relative to the anode wire can be measured. Sets of cathode strips located in front of and behind the anode wires are used for attracting positively charged ions. The strips are at an angle to the anode wires. Induction of charge on the cathode strips gives parallel position of tracks relative to the anode wire [32], [41], [42].



Figure 2.10: The drift chambers used in the GlueX experiment for charged particle tracking. On the left is the Central Drift Chamber (CDC) and on the right is the Forward Drift Chamber (FDC) [11].

2.4.4 Electromagnetic Calorimeters

Whereas the drift chambers are used for detection and reconstruction of charged particles, the electromagnetic calorimeters are used similarly for neutral particles. There are two calorimeters, the Barrel Calorimeter (BCAL) and Forward Calorimeter (FCAL) Fig. 2.11. Neutral particles are particles with no net charge such as neutrons or photons. The detection and reconstruction of photons can help reconstruct neutral mesons such as the π^0 and η . Electromagnetic calorimeters

use the pair production process to detect photons. High energy photons in a nuclear medium will pair produce into an e^+e^- pair. This pair will emit bremsstrahlung radiation and can be recorded in scintillation detectors such as the BCAL. For e^+e^- pairs that emit Cherenkov radiation, lead-glass detectors such as the FCAL can be utilized. These calorimeters detect the energy of neutral particles and also give timing information for charged tracks.

Barrel Calorimeter. The BCAL is located inside the solenoid surrounding the CDC and FDC. The BCAL is 3.9 m long with a cylindrical shape. Particles enter the BCAL and interact with thin lead sheets of about 0.5 mm in thickness that have scintillating fibers surrounding them. There are 48 modules that contain these scintillating fibers. The incoming particles excite electrons which radiate as photons. These photons are channelled through light guides to photomultiplier tubes (PMTs) which amplify the current to produce a signal. The BCAL has a range of $11^\circ < \theta < 126^\circ$ with respect to the beam axis. Position and energy information is measured by the BCAL for neutral particles as well as timing for both charged and neutral particles [32], [43].

Forward Calorimeter. The FCAL is located downstream to the TOF and is used for the forward travelling particles. The FCAL is composed of 2800 modules made of 4 cm thick lead glass blocks connected to optical cookies and new PMTs. Energy is absorbed through the blocks and detected by the cookies and PMTs. The FCAL has a range of detection for neutral particles lying in the range from $1^\circ < \theta < 11^\circ$ with respect to the beam axis. The detector itself is inside a dark room to avoid contamination of light from external sources. Neutral particles enter the detector and undergo pair production or the bremsstrahlung process. A cascading process occurs to produce “showers” of photons that are eventually detected by PMTs. The amount of the photons that are detected corresponds to the energy deposited [32], [44], [45].

2.4.5 Time of Flight

The Time of Flight (TOF) detector is important for particle identification (PID). It is composed of two planes of reflective scintillating material: one horizontal plane and one vertical plane. Each plane consists of 46 paddles. The scintillating material is designed for no light to escape. Particles hit the TOF, excite electrons which radiate photons, then the photons travel through the scintillating bars and hit PMTs. The TOF can measure the time a particle takes to travel from the interaction vertex at the ST until it hits the TOF detector. The drift chambers measure the distance travelled for charged particles which uses the timing information from the TOF to calculate



Figure 2.11: The calorimeters used in the GlueX experiment for neutral particle reconstruction and timing information. On the left is the Barrel Calorimeter (BCAL) and on the right is the Forward Calorimeter (FCAL) [11].

the velocity of charged particles. The momentum of the charged particles can be found from the bending of the particles due to the magnetic solenoid. From here, the mass can be calculated by dividing the measured momentum by the determined velocity. Masses help to determine particle identification. Given a hypothesis for a certain type of particle, there is an expected time for a particle's measured trajectory and momentum. If the assumed identity is correct, the difference between this expected time and the time information from the TOF should have a distribution that is centered near zero [46].

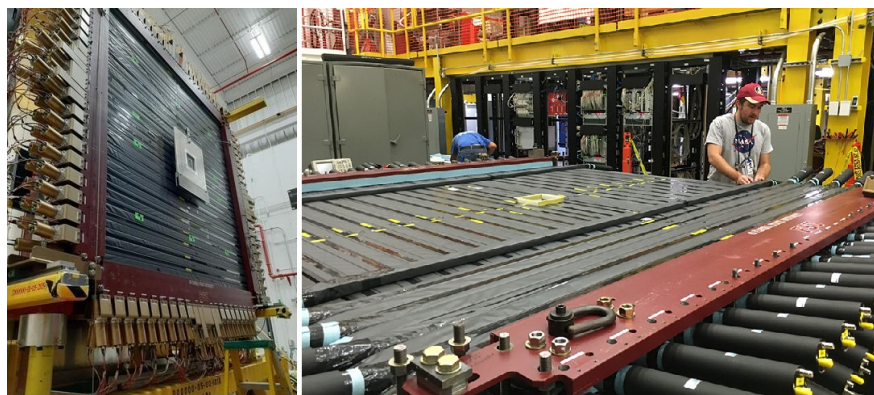


Figure 2.12: The Time of Flight detector (TOF) used in the GlueX experiment for particle identification. The left photo was taken when the TOF was mounted and experiment ready. The right photo is taken from the TOF upgrade that took place in 2019 [11].

2.4.6 Detection of Internally Reflected Cherenkov Light Detector

The Detection of Internally Reflected Cherenkov Light Detector (DIRC) is an addition to the GlueX spectrometer that was implemented in the start of GlueX Phase-II running in early 2020 Fig. 2.13. Phase II is an approved extra 400 days of data acquisition by the Program Advising Committee at Jefferson Lab. The goal of Phase II is to increase overall statistics using higher beam intensities and improve the methods of particle identification. The DIRC aids in improving PID by distinguishing pions from kaons in a wider momentum range than was possible in Phase I. This can reduce background for misidentified particles with higher momentum. It also increases the range of reactions that can be analyzed. The TOF can distinguish pions and kaons up to 2 GeV, whereas the DIRC extends this region up to 4 GeV. The DIRC is stationed between the solenoid magnet and the TOF and is made of 4 boxes containing 12 synthetic fused silica bars. Charged particles interact with the DIRC and emit Cherenkov light at a special angle called the Cherenkov angle. The velocity of the particle is inversely proportional to the cosine of the Cherenkov angle. For given momentum, particles can be identified by their Cherenkov angle [47].

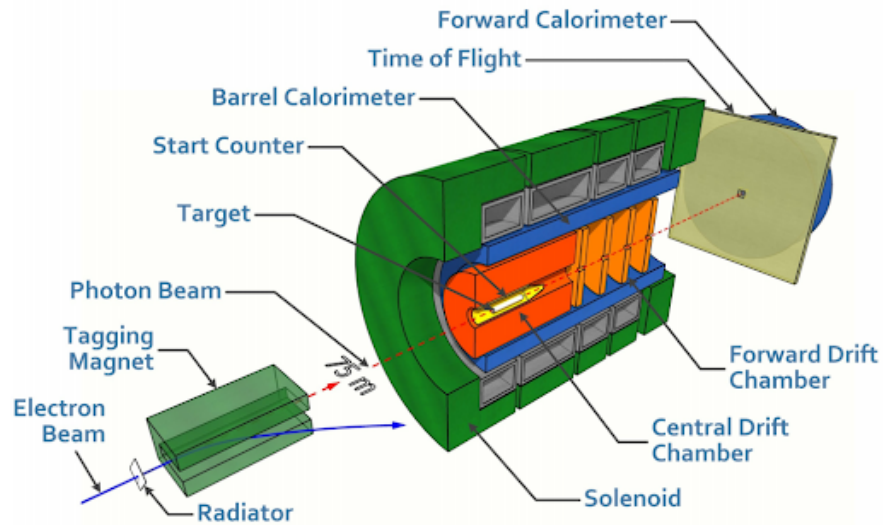


Figure 2.13: This is a diagram of the GlueX spectrometer with the Phase-II upgraded DIRC detector included. [11].

CHAPTER 3

MONTE CARLO SIMULATION FOR $\gamma\mathbf{P} \rightarrow \eta'\eta \mathbf{P}$

Monte Carlo (MC) simulation is important in order to understand detector acceptance and get an idea of what to expect in data samples. The first step of the process is the generation of four-vectors of the various particles present in the reaction. For this process, a software called genr8 is used. To generate these events, a beam energy range is specified as well as a t -slope where t is the Mandelstam variable. The Mandelstam variable t distribution is given by the relationship $t = (p_1 - p_3)^2 = (p_2 - p_4)^2$ and is described by the figure below [4]. The final state particle kinematics are documented in an input file to tell genr8 what sort of processes to include. Masses and widths of the final state particles are specified along with the decay process. The run period and run numbers are specified for generation so that the generator can pull exact information when generating events. This is helpful to make accurate comparisons with the data.

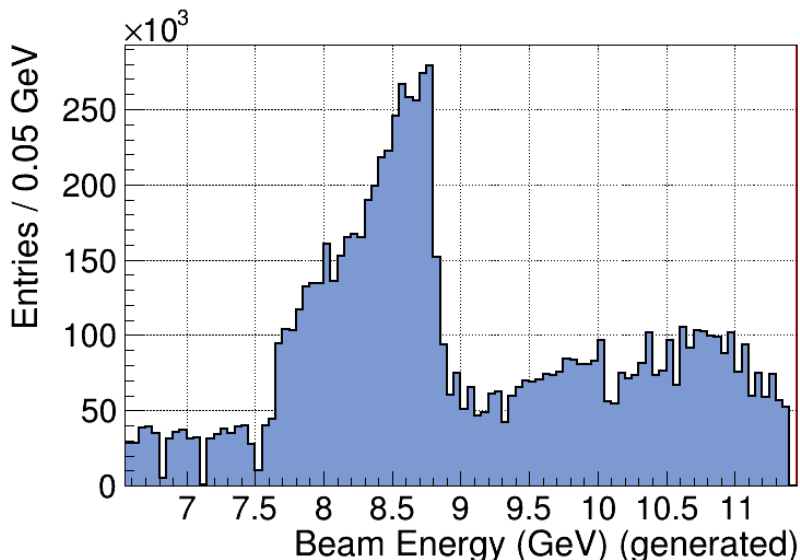


Figure 3.1: The beam energy distribution for generated Monte Carlo. The beam energy was generated for a range of 6.5 to 11.4 GeV. The coherent peak is maximal near an energy of 8.8 GeV.

After the events are generated, the four vectors are passed through a software that simulates detector geometry and acceptance. These reconstructed MC events are used to calculate the MC

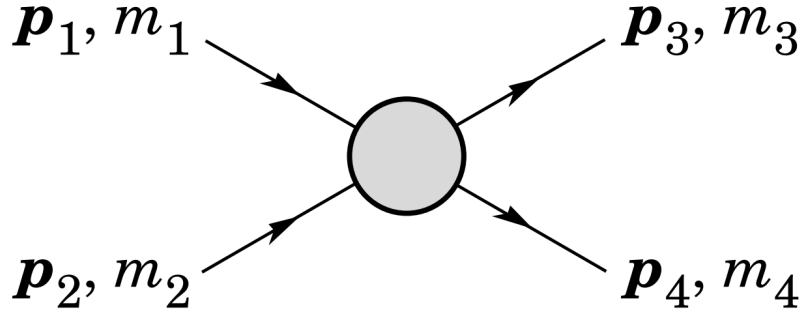


Figure 3.2: This diagram shows particles p_1 and p_2 interacting to produce particles p_3 and p_4 . Imagine in this case for p_1 to be the photon beam, p_2 to be the target, p_3 is $\eta\eta'$ and p_4 is the recoil proton.

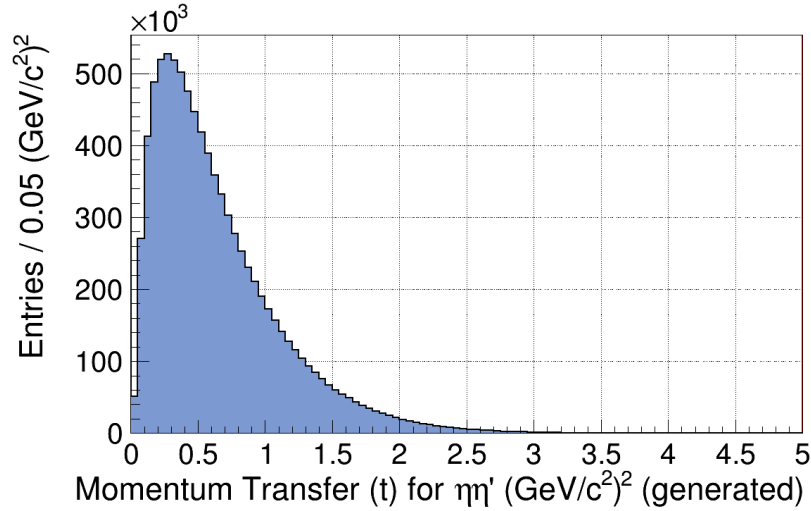


Figure 3.3: The Mandelstam variable $-t$ distribution, also referred as momentum transfer, for generated Monte Carlo. The slope generated for this process is $2.6 (\text{GeV}/c^2)^2$.

efficiency which is the fraction of events that are detected and that remain after data selections. This is calculated by dividing the accepted events that pass through the detector geometry and acceptance by the generated events. These accepted events will also have the same data selection criteria applied as the data. This will be used for calculating a total cross section measurement which will be discussed in a later section.

When simulating MC events, their software versions must match with the data software versions in order to properly make comparisons. These versions as noted at the beginning of the previous chapter can be specified as an input for generation. For this analysis, the reaction $\gamma p \rightarrow \eta'\eta p$ was simulated where $\eta' \rightarrow \eta\pi^+\pi^-$ and $\eta \rightarrow \gamma\gamma$ for both *etas*. 10 million events were generated for each

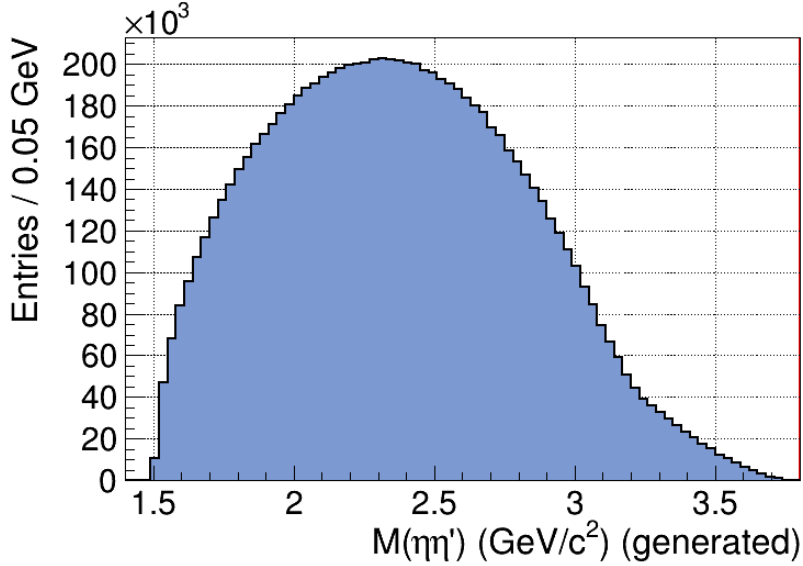


Figure 3.4: The generated mass for the η'/η final state.

of the run periods in GlueX Phase-I: 2017, 2018-01, and 2018-08. The plots shown here are for the 2018-08 run period. The beam energy range used for simulation was from 6.5 to 11.4 GeV. These events were generated with a $-t$ -slope of $2.6 \text{ (GeV}/c^2)^2$. There was no information for the spin of the parent or daughter states for the final state phase space.

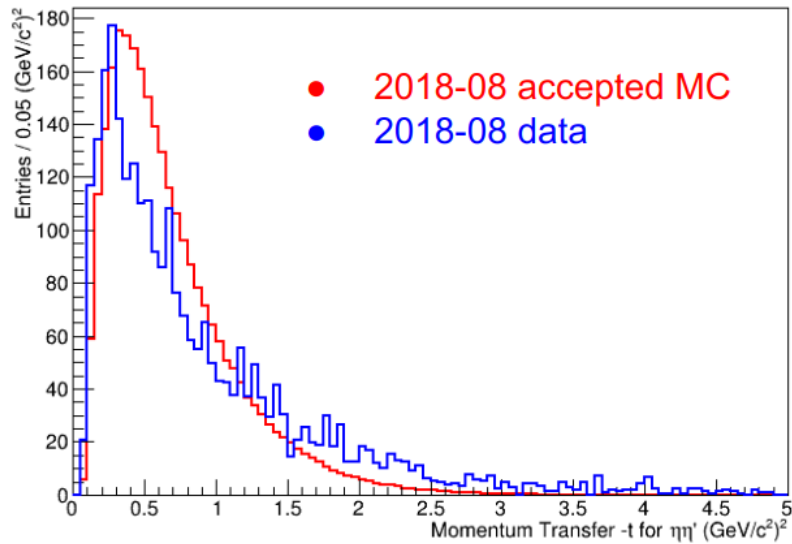


Figure 3.5: The normalized Momentum transfer $-t$ -distributions for accepted Monte Carlo (in red) and data (in blue). The data and MC are both using the entire run range for the 2018-08 run period.

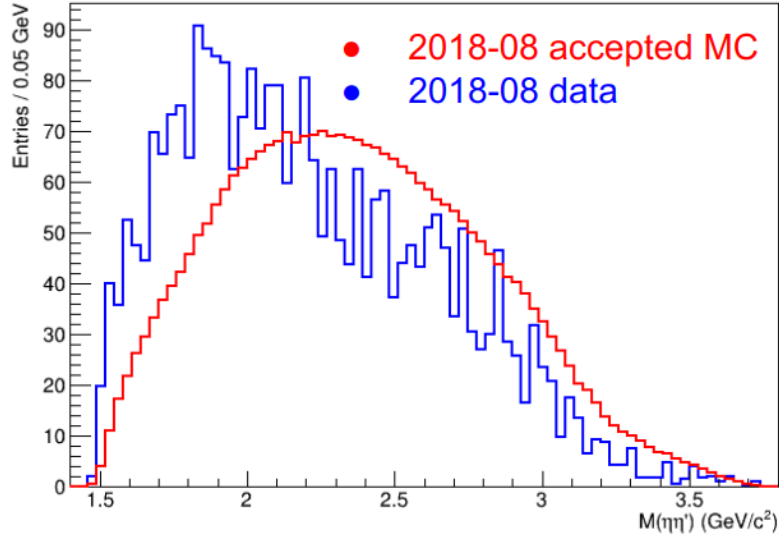


Figure 3.6: The normalized mass distributions for the $\eta'\eta$ final state for accepted Monte Carlo (in red) and data (in blue). The data and MC are both using the entire run range for the 2018-08 run period.

In order to ensure proper calculations for efficiencies, the events must be simulated that represent data accurately. This means that multiple iterations are necessary for good MC samples. Shown below are the data/MC agreements for the $-t$ distributions. In the plot to follow these, $M(\eta'\eta)$ for the 2018-08 data set is compared with the reconstructed MC to show their agreement of phase space. These are plotted from reconstructed MC, after passing all the same selections as the data which will be discussed in the next chapter.

CHAPTER 4

DATA SELECTION

The goal of the analysis presented in this dissertation is to achieve an exclusive $\eta'\eta$ final state. This is the first analysis that has explored photoproduction of $\eta'\eta$. An estimate of total signal events will be presented for t-channel production along with a cross section calculation in bins of mass of $\eta'\eta$. To begin, a discussion on the data used from the GlueX experiment will be discussed.

There are three running periods that make up the GlueX Phase-I data: Spring 2017, Spring 2018, and Fall 2018. For each of these run periods, data was taken over a series of “runs”. The run numbers that are included in each of these run periods are given in the table below Fig. 4.1:

Table 4.1: Run periods with their run range for the GlueX Phase-I data.

Run Period	Run Range
Spring 2017	30274 - 31057
Spring 2018	40856 - 42559
Fall 2018	50685 - 51768

During these run periods a total of about 50, 150, and 80 million reconstructed events were collected, respectively, corresponding to 18%, 54%, and 29% of the full GlueX-I data. Each run was up to two hours in length and the diamond orientations were switched between runs. Using the lab floor as a reference, the diamond radiator was set at 0 deg, 45 deg, 90 deg, or 135 deg. Different orientations are used for calculating observables that are polarization-dependent such as the beam asymmetry. These orientations are also used to cancel out azimuthal asymmetries by using perpendicular pairs of data sets. After a certain number of triggers was taken for a certain orientation, the diamond’s orientation was changed. An amorphous radiator was also used as a control.

For the analysis procedure, examples are provided using only the Fall 2018 data set for simplicity. The same procedure is applied on the other run periods and the final results will be shown by combining all three. The reconstructed data trees contain four photons, a π^+ , a π^- , and a recoil proton. The two photon pairs are restricted to lie within a mass window of 0.35 to 0.75 GeV/ c^2 . The data selection procedure will identify $\eta \rightarrow 2\gamma$ for two η s as well as $\eta' \rightarrow \eta\pi^+\pi^-$.

4.1 Kinematic Fitting

The overall goal of the data selection is to achieve an exclusive reaction of $\gamma p \rightarrow \eta' \eta p$. For this reaction to be exclusive, all of the particles should be measured and none should be missing. A helpful tool for achieving exclusivity is a procedure called kinematic fitting [48]. For a certain reaction, this procedure modifies the four-vectors of the measured particles to satisfy a set of imposed constraints. By using the kinematically fitted four-vectors, the resolution of the measured particles is improved. This procedure is also useful in eliminating final state events that are a result of a different final reaction. The kinematic fitting used in this data set enforces energy and momentum conservation and vertex constraints. The vertex constraint requires all charged particles in the reaction to come from the same place. This is done by using a Lagrange Multiplier approach. The goal is to find the best estimation of the final state four momenta. This is done by calculating the minimum on the χ^2 value in the following equation:

$$\chi^2 = (y - \beta)^T V^{-1} (y - \beta) - 2\lambda^T f(\beta, \dots). \quad (4.1)$$

Here β are the inputted four momenta for the final state particles, y is the best estimation of the four momenta, V is the covariance matrix that represents the detector resolution, λ is the Lagrange Multiplier that implements the conservation of four momentum constraint, and $f(\beta, \dots)$ is the function describing the conservation of four momentum [49]. This is an iterative method. Events that don't converge are discarded as it is a sign that they belong to a different final state hypothesis. The χ^2 value reflects how well the measured particles match the hypothesis. Small values indicate a minimal modification of the measured vectors. These events have a higher likelihood to be from the final state that was hypothesized at the beginning of the procedure. A Confidence Level cut which is equivalent to a χ^2 cut will be used later in this analysis to enforce exclusivity. The Confidence Level is related to the χ^2 distribution linearly.

4.2 Stage 1

At this stage of the analysis, there is a lot of background in the data that can be removed with cuts that require little amount of study. There are multiple combinations per event remaining after applying these cuts. The multiplicity of combos in an event comes primarily from the multiple beam hypotheses and not from the final state particles.

The FCAL shower quality factor is a probability if showers are being produced electromagnetically. For values close to one, there is a higher confidence that these showers are from photons. A standard cut for the FCAL shower quality factor is used that throws out events with a quality factor less than 0.5 Fig. 4.1.

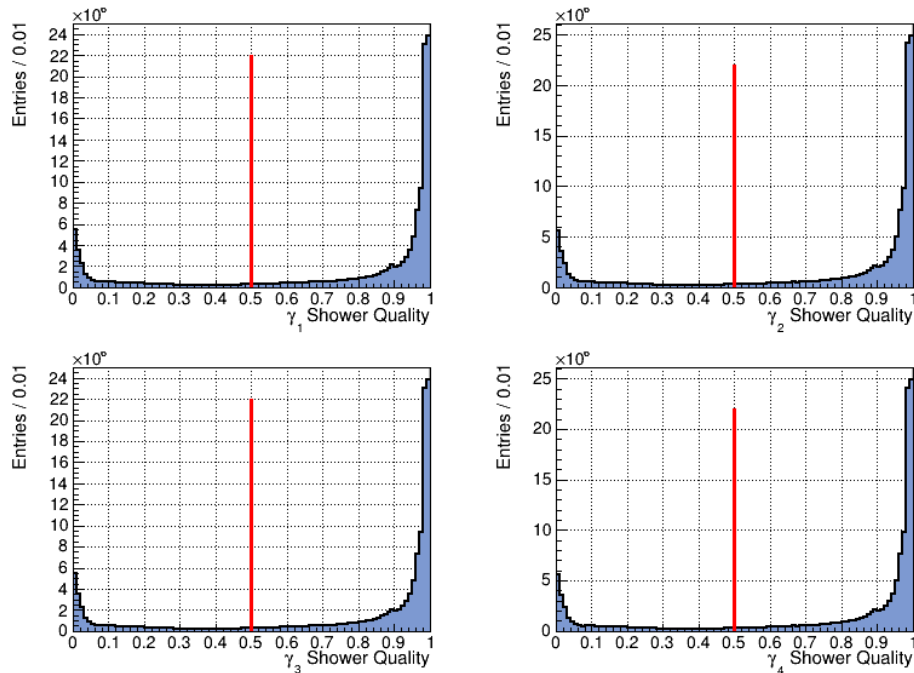


Figure 4.1: The red line shows the value of the cut imposed on the FCAL shower quality factor. Events are kept to the right of this line, while the events to the left correspond to showers that are unlikely to come from photons and are thrown away.

The next step is to separate beam bunches in accordance with their timing distributions. This is done by calculating the change between the radio frequency (RF) time and the beam time. The RF time is the time when the beam enters the hall. This is well known since the electron beam bunches are sent every 4 ns. The beam time is the time when reconstruction converged to a common vertex time. This common vertex time is calculated by tracing back from final state particles to a common point by using their charged tracks and timing information.

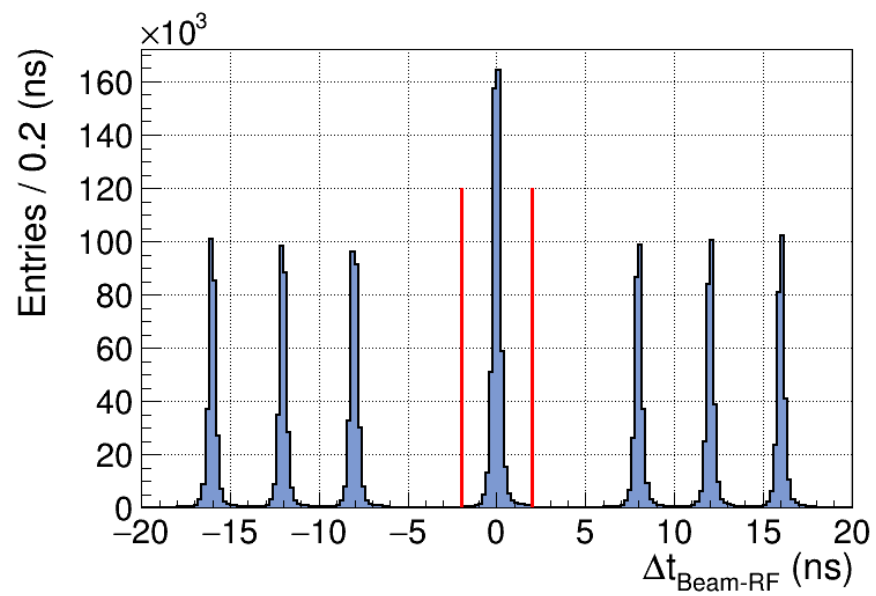


Figure 4.2: The selected beam bunch lies between the red lines. The other beam bunches will be used later to subtract accidentals in the analysis. The two peaks nearest to the central peak are omitted to avoid leakage into the central peak.

From this information, the beam bunches that are within 2 ns from 0 are selected. These are considered to be the in-time bunches. The out-of-time beam bunches are the remaining peaks that lie farther than 2 ns from 0 and are called accidentals. These are still of interest and will be used later on to perform accidental subtraction. This is a process that will be discussed later on in detail Fig. 4.2.

From here the target can be identified. To do this, the vertex position for the radial direction is restricted such that the proton is within the target chamber. The z-vertex distribution is restricted to be within a standard range of 52-78 cm. Fig. 4.3. These values are chosen from studies performed by Austregesilo et. al. [50].

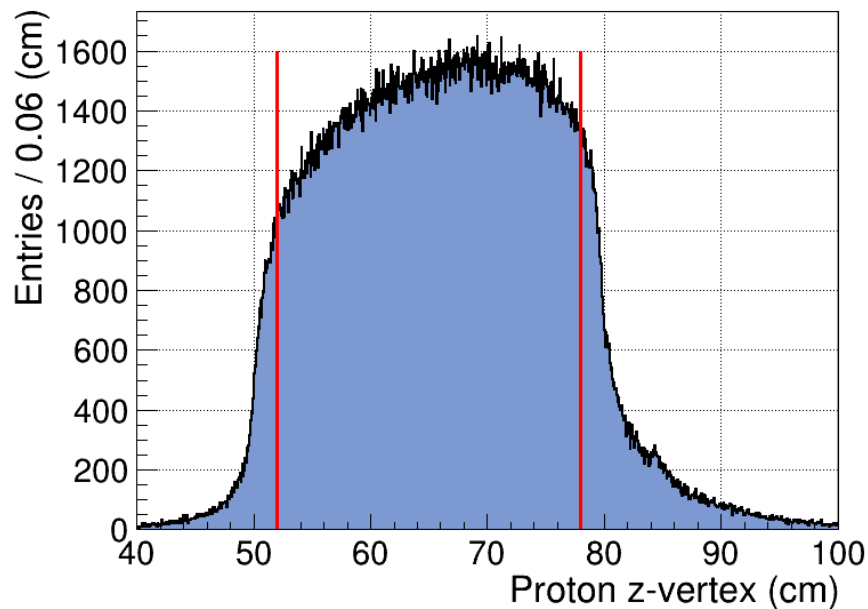


Figure 4.3: The events lying in the range between the red lines for the target chamber are kept.

There is still significant background in the data. In order to perform meaningful studies, a cut that removes a large portion of this background is necessary. The confidence level gives information on how likely it is for a combination to come from the reaction of interest with values ranging from 0 to 1. Removing any combinations that has a low probability to be of interest can remove a lot of background. A cut is performed on the confidence level removing any combination with a confidence level value less than 1×10^{-2} . After choosing an optimal π^0 removal, the confidence level will be revisited where a study will be performed to choose an optimal confidence level value

to cut on Fig. 4.4. This study is not performed at this stage because an exclusive reaction should be achieved before determining an ideal confidence level cut.

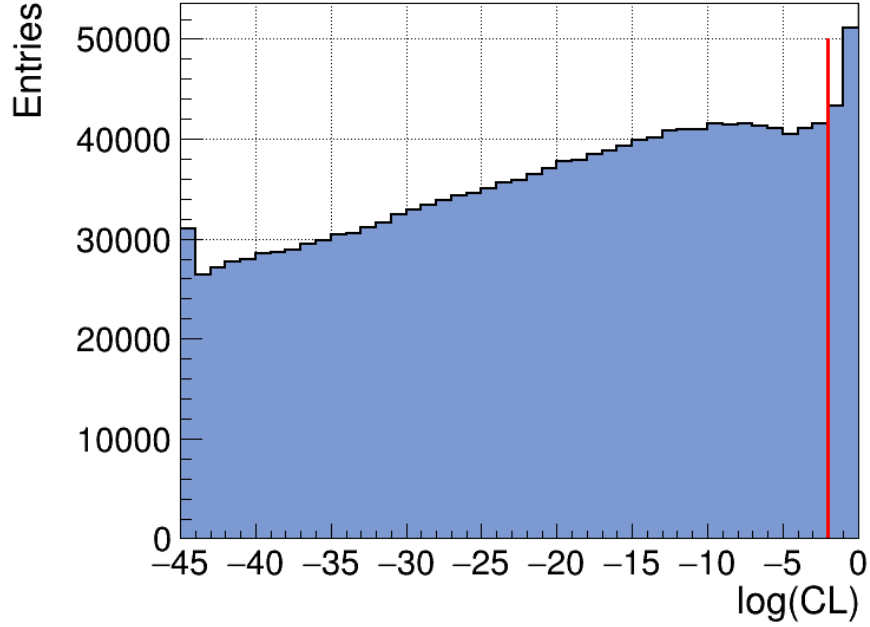


Figure 4.4: The red line shows the value of the cut imposed on the Confidence Level, which is a variable that relates how likely a combination is to come from the reaction of interest. Events to the right of the red line are kept which have a higher confidence of resulting from the reaction of interest.

At this stage the goal is to select exclusive η s. There is significant background coming from π^0 s. The main goal for this stage is to remove background coming from the reaction $\gamma p \rightarrow \pi^0 X \pi^+ \pi^- p$.

There are two η s in the reaction, where each of the η s decay to two photons. Thus, there are four photons total in the final state. The four photons can be arranged in two pairs three different ways. Combinations of photon pairs that lie within an η mass region of $(0.35, 0.75) \text{ GeV}/c^2$ are kept corresponding to the pair $\gamma_1\gamma_2$ and the pair $\gamma_3\gamma_4$, where the labels of the photons are only important to keep track of ordering. However, photons from other combinations that come from π^0 s can fall into this η mass region. The $M(2\gamma)$ distributions for photons from these other combinations show there is a clear peak that shows up near the π^0 mass of $0.135 \text{ GeV}/c^2$ Fig. 4.5. A study was performed to find the optimal cut for removing these π^0 s. To choose an optimal cut for removing the π^0 s, an estimate of how many good η s was taken as the π^0 removal range was varied.

The two photon mass distributions are fitted with a Gaussian for the π^0 signal and a 1st order polynomial for the the background. Two Gaussian distributions are necessary to accurately describe

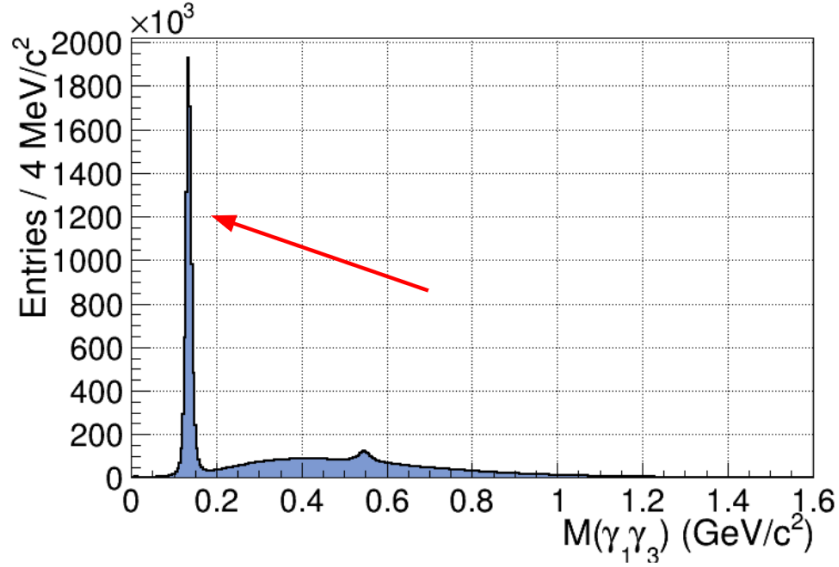


Figure 4.5: An example of a combination pairing of two photons, $\gamma_1\gamma_3$, where a π^0 peak is clearly visible as directed by the red arrow.

the π^0 signal that is present in our data due to the different resolutions of the two calorimeters Fig. 4.6.

The parameter values are extracted from the fits to determine the mean and standard deviation for the combined Gaussian distributions. Any events that contain two photons lying within a mass range of the π^0 are removed. This mass range is varied from 1σ up to 5σ in increments on 0.5σ . After the cuts are applied, both the $M(2\gamma)$ distributions chosen to be the two η candidates are considered. They are modeled using two Gaussian distributions for the η signal with a 3rd order polynomial to model the background Fig. 4.7. Two Gaussian distributions are used to model the two detector resolutions, by the same argument earlier.

An estimation for the signal and background for these distributions over a 2σ mass range for the η s was computed. From this, the significance is calculated which is given by the ratio of the number of signal events divided by $\sqrt{signal + background}$ for different values of cut ranges for π^0 removal Fig. 4.8. The distribution peaks at maximum significance using a π^0 removal range of 3σ which will be the range to be used moving forward to the next stage.

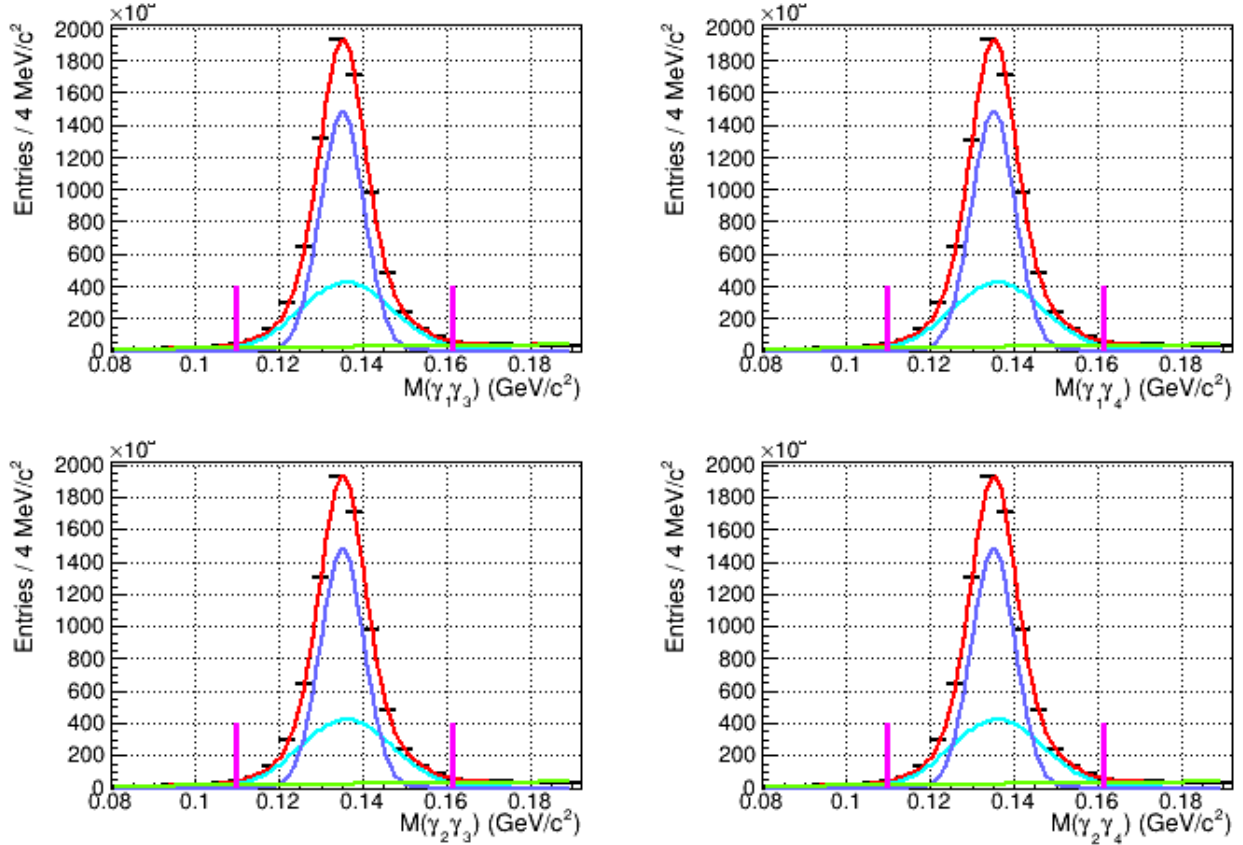


Figure 4.6: Shown above are two-photon combination masses that contain π^0 contamination. The mass distributions are fitted with two Gaussian distributions added to a 1st order polynomial. The red distribution is signal plus background, the purple and blue distributions are the two Gaussian distributions, and the green distribution is the polynomial background. The magenta lines correspond to a 3σ range calculated from the fits.

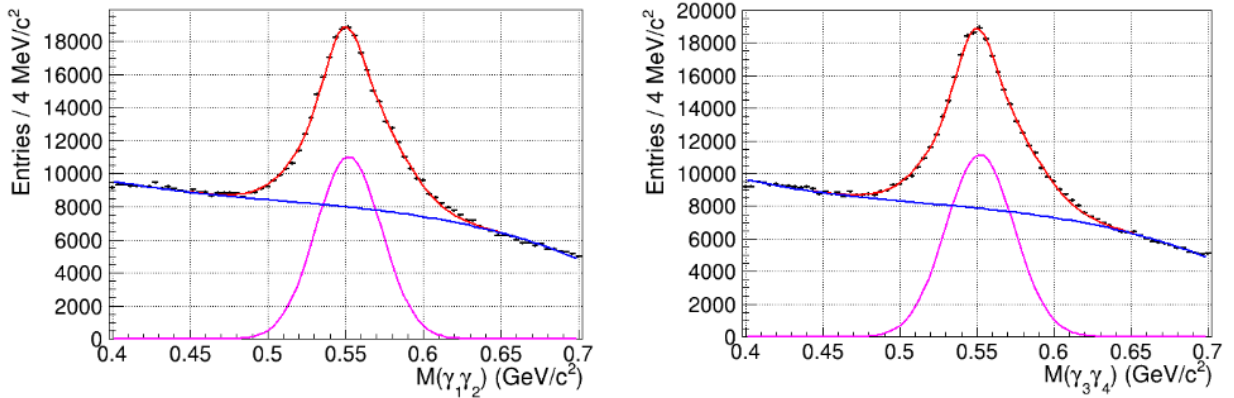


Figure 4.7: Shown above are the two η candidates after applying a 3σ π^0 removal. These candidates are fit with two Gaussian distributions plus a 3rd order polynomial.

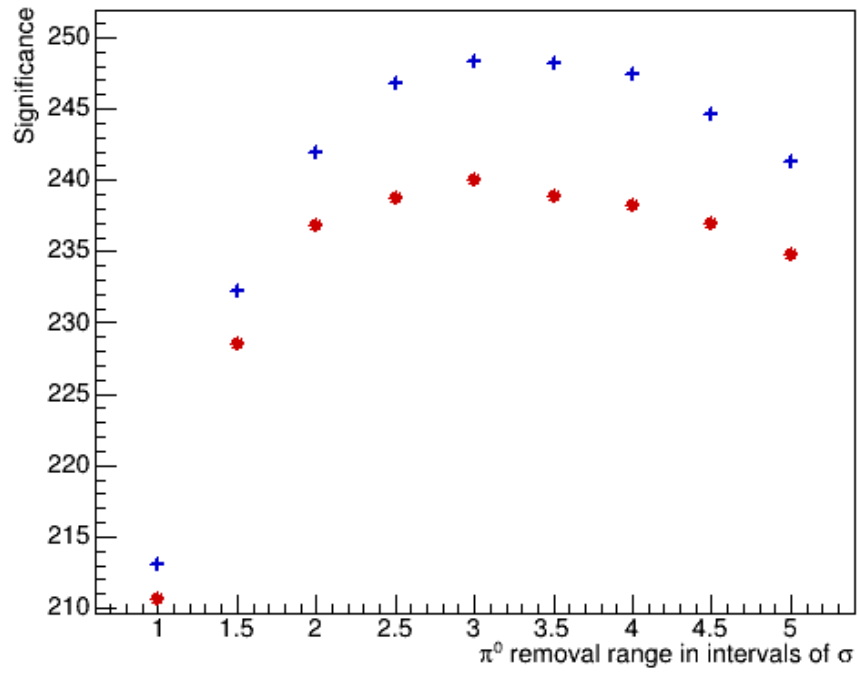


Figure 4.8: Plotted is the significance for the two η candidates as a function of π^0 removal from 1σ up to 5σ in increments of 0.5σ . The significance peaks at the π^0 removal range of 3σ .

4.3 Stage 2

After removing events that have π^0 s, cuts are performed on the Missing Mass Squared (MMS) and Missing Energy (ME) distribution tails. Cutting on these quantities will remove events that do not obey conservation of four-momentum in the reaction. First, the tails of the MMS distribution are removed, keeping only events that lie within $(-0.04, 0.04) (\text{GeV}/c^2)^2$ Fig. 4.9. The ME is fitted using a Gaussian distribution added to a 1st order polynomial. The mean and standard deviation are extracted from the Gaussian fit and a cut is applied on the tails of the distribution removing events that lie outside of a 3σ window Fig. 4.11. A comparison with signal Monte Carlo is also presented to ensure that signal events are not being removed. The distributions in signal Monte Carlo do not include any background, so they will not agree entirely with the data Figs. 4.10, 4.12.

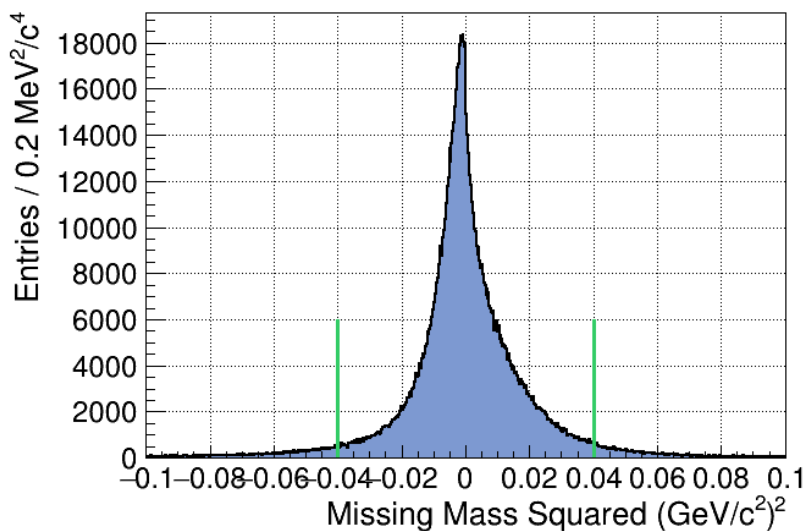


Figure 4.9: Missing Mass Squared distribution. The green lines indicate the removal of the tails outside of the range $(-0.04, 0.04)(\text{GeV}/c^2)^2$.

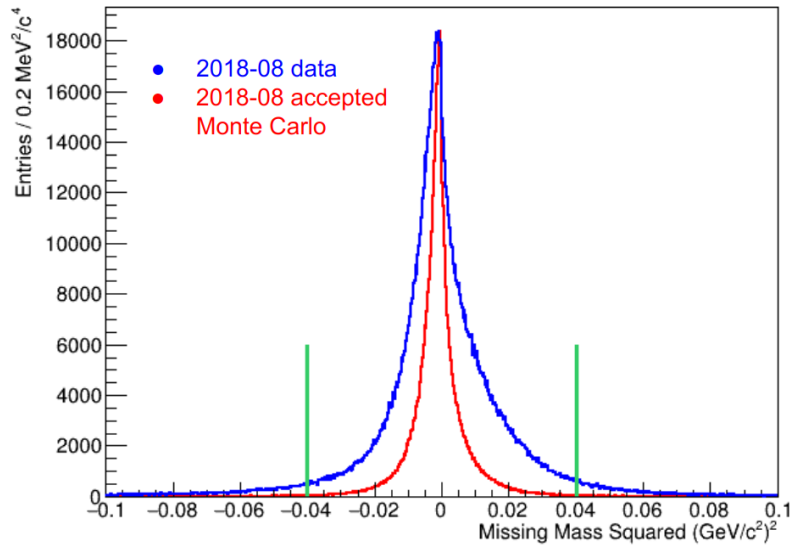


Figure 4.10: Missing Mass Squared distribution in both data and signal Monte Carlo. The Monte Carlo distribution is normalized to the maximum number of entries in the data. The green lines indicate the removal of the tails outside of the range $(-0.04, 0.04)(GeV/c^2)^2$.

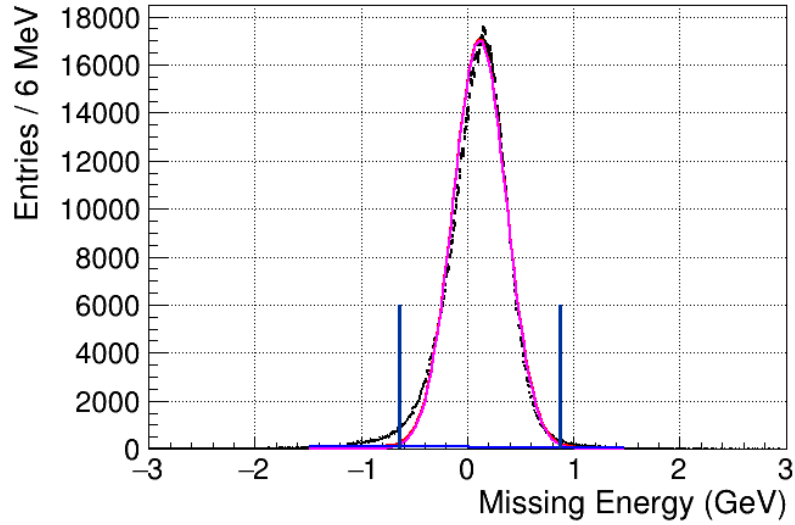


Figure 4.11: Missing Energy distribution. The blue lines indicate the removal of the tails outside of a 3σ window.

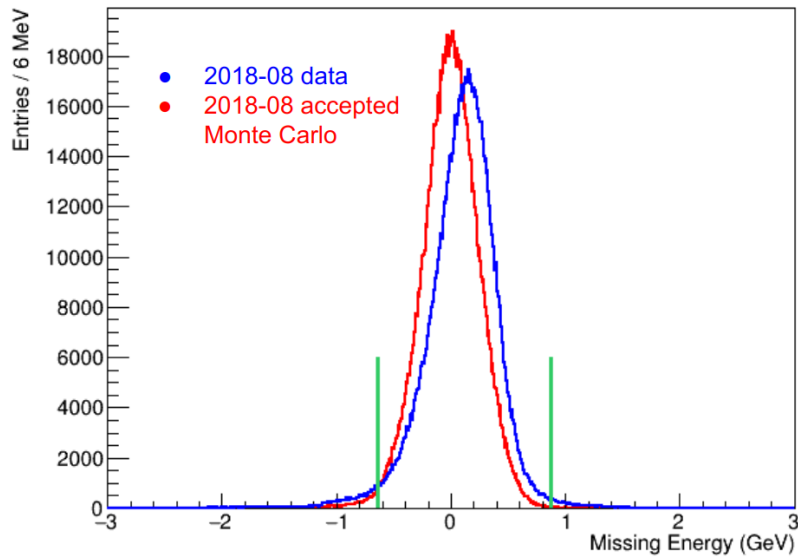


Figure 4.12: Missing Energy distribution in both data and signal Monte Carlo. The Monte Carlo distribution is normalized to the the data. The green lines indicate the removal of the tails outside of a 3σ window.

4.4 Stage 3

As mentioned earlier, there are two η s in the reaction of interest. Plotting a two-dimensional distribution of the two η candidates, shows there is an overlap region near the center where the

signal is located. Using the fits performed in Stage 1 for the two η candidates Fig. 4.7, different selections are applied on the two-dimensional distribution to find the optimal one. The selections range from 1σ up to 4σ in increments of 0.5σ Fig. 4.13. To find the percentage on signal to background, $M(\eta\pi^+\pi^-)$ (GeV/c^2) is fitted for the η' with a Gaussian distribution for the signal and a 3rd order polynomial for the background Fig. 4.14. Calculating the background percentages and total amount of signal and background events for each of the selections, the significance is plotted Fig. 4.15. The distribution peaks near the 1.5σ and 2σ selections. The background reduces from 34% to 25% between these selections. In terms of total number of events, the number of signal events is reduced by 9% and the number of background events reduced by 40%. Since the reduction of background is so significant, the 1.5σ selection is performed.

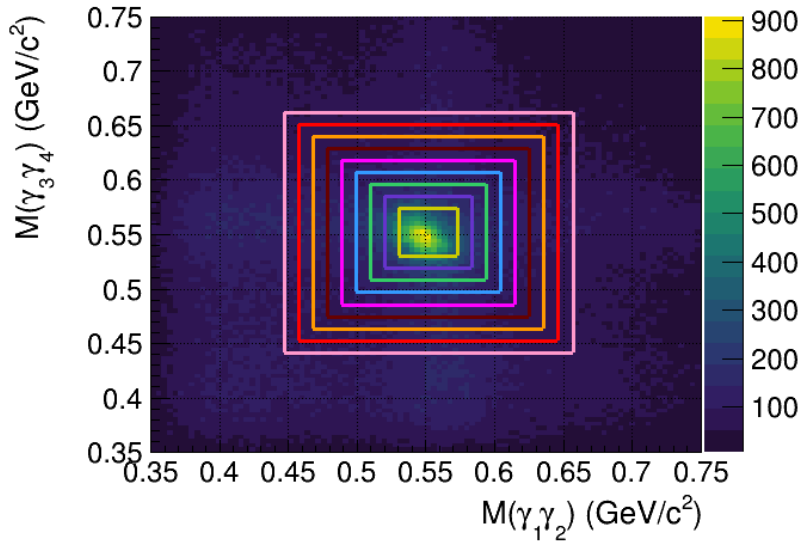


Figure 4.13: Plotted is the two-dimensional distribution of the mass of the two η candidates. The colored boxes represent the list of selections applied which range from 1σ up to 4σ in increments of 0.5σ .

4.5 Stage 4

A cut is implemented on the $M(\pi^+\pi^-)$ distribution, removing events greater than $0.42 \text{ GeV}/c^2$. Removing these events does not affect the events in the region of η' as seen in the two-dimensional plot Fig. 4.16.

The GlueX beam has a coherent peak that lies between 8 - 9 GeV. In order to focus at energies high enough to separate production of baryon and meson resonances, a beam energy selection is

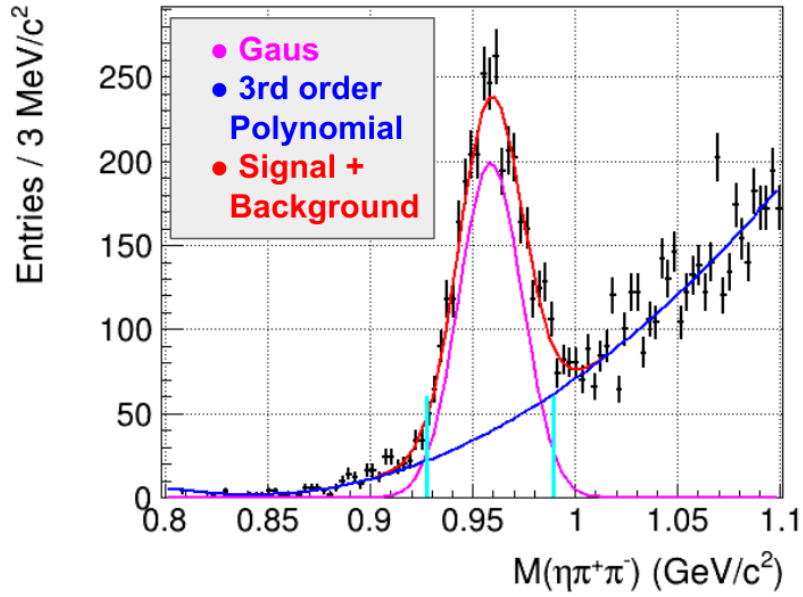


Figure 4.14: Plotted is the $M(\eta\pi^+\pi^-)(GeV/c^2)$ after making a two-dimensional 1.5σ η selection. The distribution is fitted with Gaussian for the signal and a 3rd order polynomial for the background.

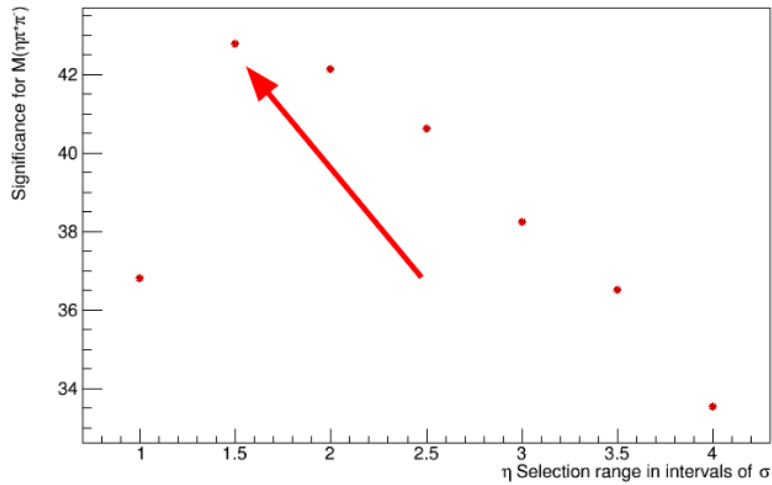


Figure 4.15: Plotted is the significance for the $M(\eta\pi^+\pi^-)$ as a function of a two η selection ranging from from 1σ up to 4σ in increments of 0.5σ . The significance peaks near 1.5σ and 2σ

performed that keeps events that lie near or above the coherent peak. The beam energy cut removes events less than 7.5 GeV Fig. 4.17.

The Confidence Level is revisited to optimize the selection of $\eta\eta'$. The cuts are varied removing

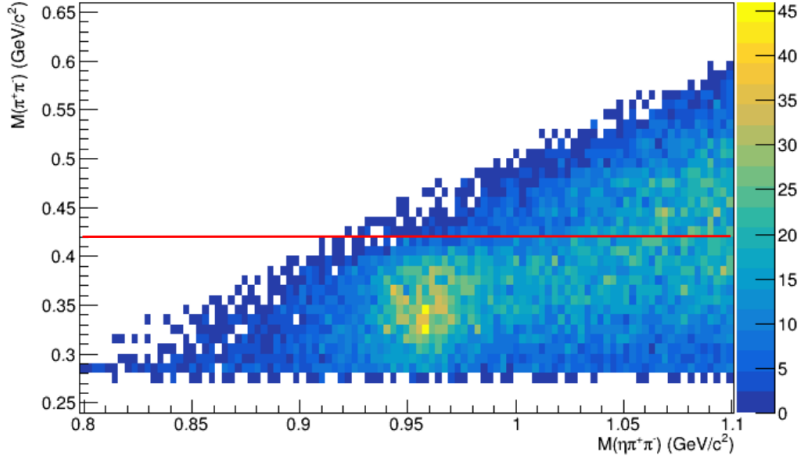


Figure 4.16: The $M(\pi^+\pi^-)$ distribution is cut for events greater than $0.42 \text{ GeV}/c^2$.

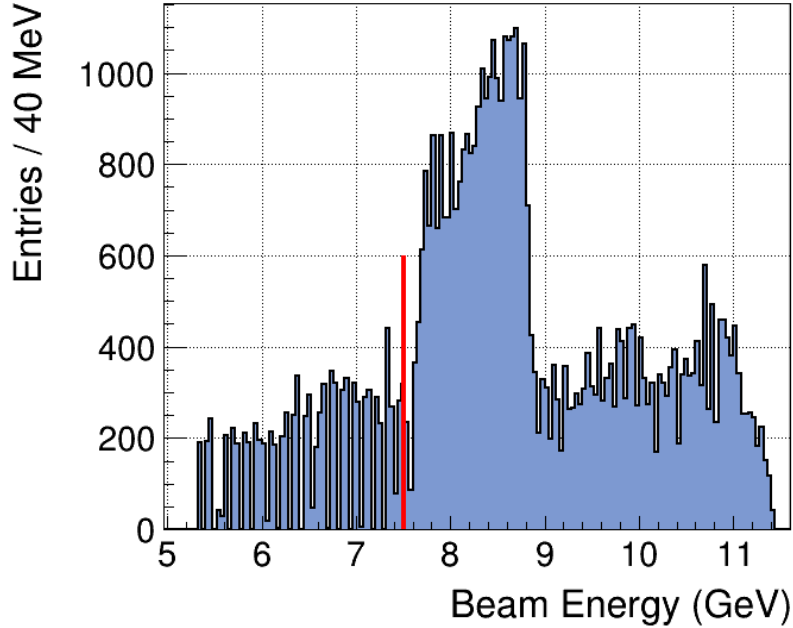


Figure 4.17: The beam energy distribution is selected to be above 7.5 GeV since the analysis focuses on meson production near or above the coherent peak.

events that have confidence level less than 10^{-20} , 10^{-19} , ..., 10^{-1} reducing the value by powers of 10 each time. Events are removed that have a confidence level less than these values. The signal, background and significance for each cut is calculated by fitting the $M(\eta\pi^+\pi^-)$ distribution similar to the previous stages. It is noted that this value of the Confidence Level is much looser than the removal of events that have confidence level less than 10^{-2} which was used in the earlier stages.

The significance peaks when events are removed with confidence level values less than 10^{-9} . At this stage, about 63% of our total η' events correspond to signal events. Fig. 4.20. A comparison with signal Monte Carlo is also presented 4.18.

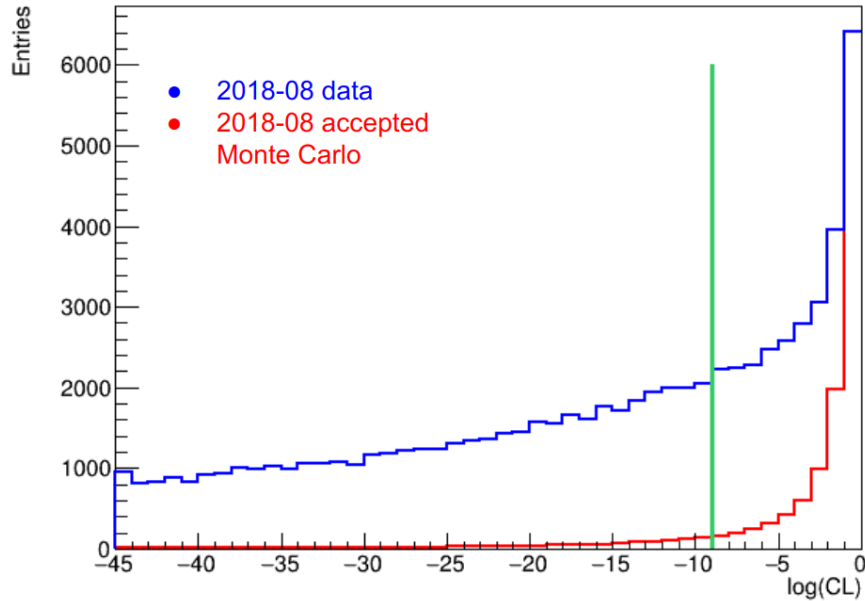


Figure 4.18: The Confidence Level which relates how likely a combination is to come from the reaction of interest. Events to the right of the green line are kept which have a higher confidence of resulting from the reaction of interest. Data is shown in blue, while signal Monte Carlo is presented in red.

4.6 Stage 5

At this stage, selecting the η' is necessary in order to achieve the $\eta'\eta$ final state. Since there are two η s in the reaction, either of these could potentially decay from the η' . A 2σ selection is made to select the signal region in the $M(\eta\pi^+\pi^-)$ distribution, where a Gaussian along with a 3rd polynomial is fitted to model the signal and background respectively. In the region where both $M(\eta\pi^+\pi^-)$ distributions overlap for the signal selection, each η' candidate is checked to see which has a mass closest to the accepted value as mentioned by the Particle Data Group (PDG) value of the mass of η' . The one that has a mass closest to the PDG value is chosen in this region Fig. 4.21. The next step will be to see which other types of reactions are present in the analysis.

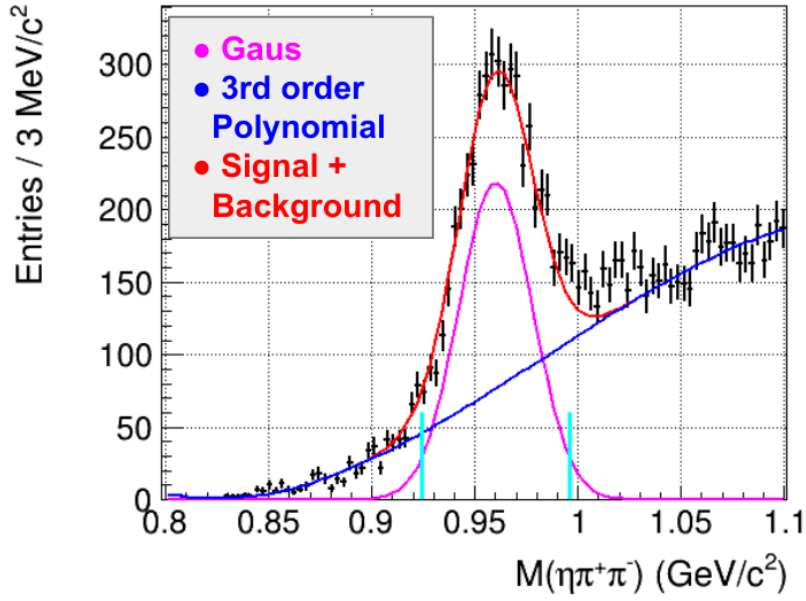


Figure 4.19: Plotted is the $M(\eta\pi^+\pi^-)$ (GeV/c²) after removing events with confidence level values less than 10^{-9} . The distribution is fitted with Gaussian for the signal and a 3rd order polynomial for the background.

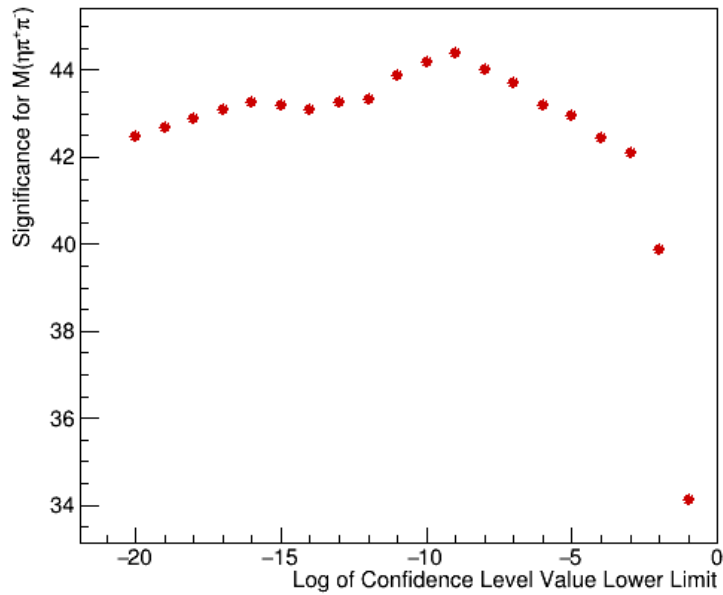


Figure 4.20: Plotted is the significance for the $M(\eta\pi^+\pi^-)$ as a function of confidence level cut values ranging from 10^{-20} , 10^{-19} , ... 10^{-1} . The significance peaks near a value of 10^{-9} .

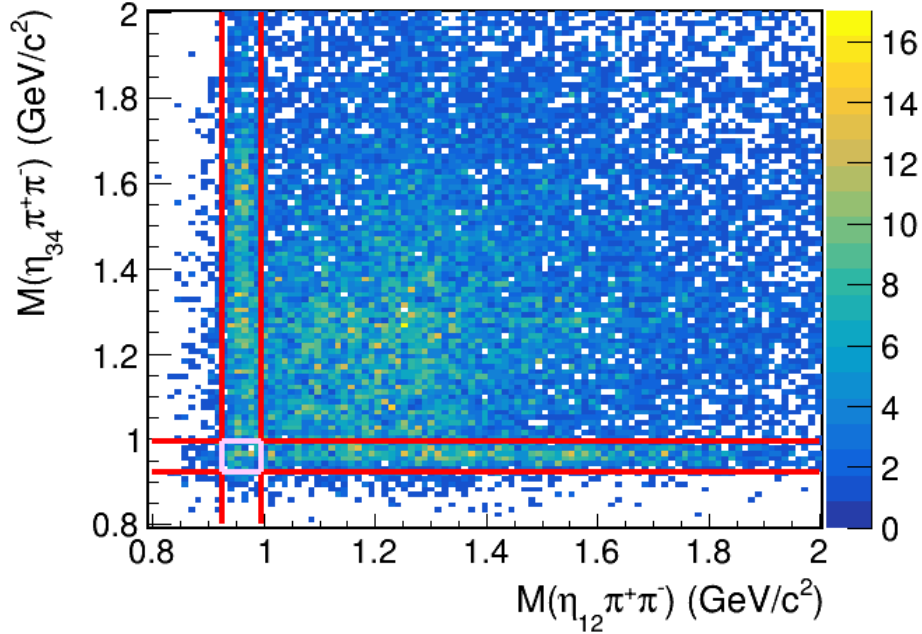


Figure 4.21: Selecting the η' for the reaction. There are two η s present, so there are two choices.

4.7 Stage 6

By plotting the $M(\eta p)$, a significant contribution from an N^* resonance is observed, namely the $N(1535)$ which results from the reaction $\gamma p \rightarrow \eta \pi^+ \pi^- N^*$ where $N^* \rightarrow \eta p$. This is not a process of interest, so a mass cut is applied to remove events less than $1.65 \text{ GeV}/c^2$ in $M(\eta p)$ Fig. 4.22. This is the most significant N^* contribution in the reaction and relates to events in the higher mass region of $M(\eta' \eta)$ Fig. 4.23. There may be some others lying in a higher mass range of $M(\eta p)$, however distinguishing these from the signal is quite difficult. Due to the limited statistics of the $\eta' \eta$ channel, the signal should be preserved as much as possible.

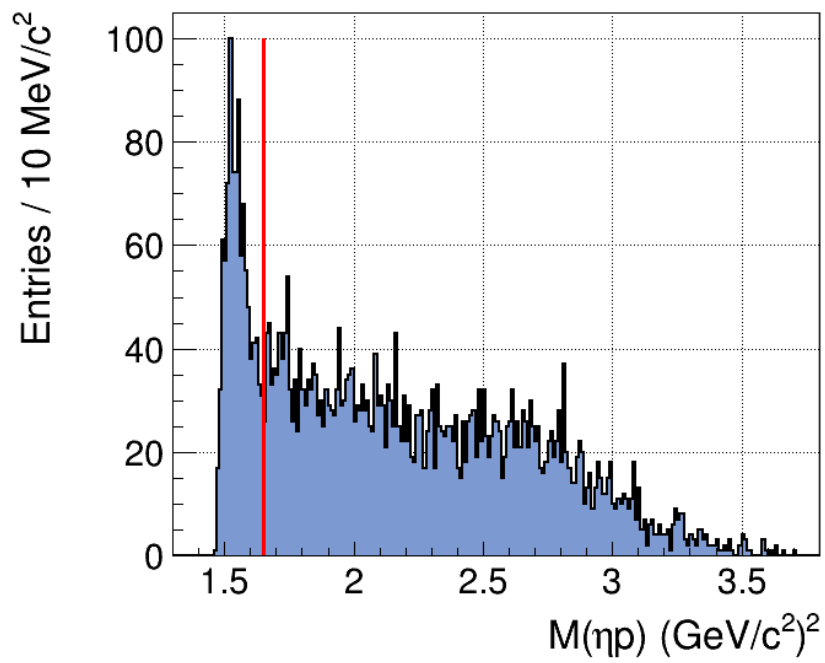


Figure 4.22: By plotting the $M(\eta p)$ selecting the bachelor η , there is a clear N^* resonance corresponding to the $N(1535)$ that is present in the data. Events to the left of the red line are removed.

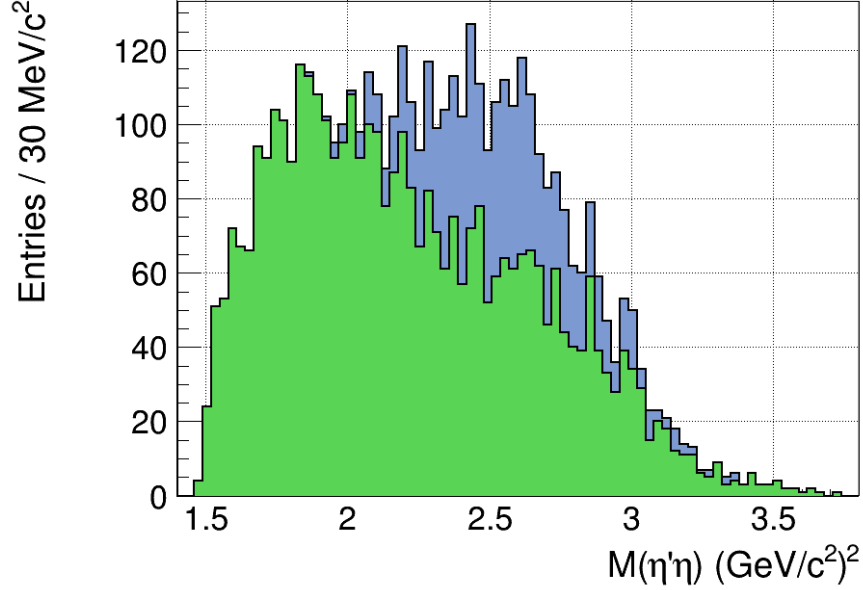


Figure 4.23: After removing the N(1535) from the data, the $M(\eta'\eta)$ is plotted before and after the removal. The blue shaded region is before the removal and the green shaded region is after removal. Clearly, the N(1535) events are seen in the higher mass region of the $M(\eta'\eta)$. It is noted that there is 33% background estimated under the η' .

4.8 Stage 7

At this stage, there are still multiple combinations per event remaining primarily from the multiple beam hypotheses Fig. 4.24. At a given time, the electron beam sends multiple electrons that interact with the diamond radiator. Some of these electrons produce photons. The energy of the recoil electrons is measured and sometimes they have very similar energies. It's difficult to distinguish which of these electrons produced a photon that ended up causing the reaction to occur at the target and producing an event. The photons that did not cause the reaction to occur are labelled accidentals and contribute to extra combinations in the data. Accidental subtraction is a way to deal with these extra combinations. This is done by artificially linking out-of-time photons with an event. The off-time candidates are used since it is known that they didn't produce the reaction, but it tells us how likely we are to assign a photon with similar energy to a reaction. This gives a good estimate of how many extra combinations are in the event. These out-of-time events are then given a negative weight and subtracted from the primary beam bunch centered at zero. In the data, four out-of-time beam bunches have been kept on either side of the primary peak. The

first beam bunch on either side is ignored in the accidental subtraction since some of these events may leak into the primary peak Fig. 4.25. At this stage of the analysis there are about 67% events remaining under the $M(\eta\pi^+\pi^-)$ distribution Fig. 4.26.

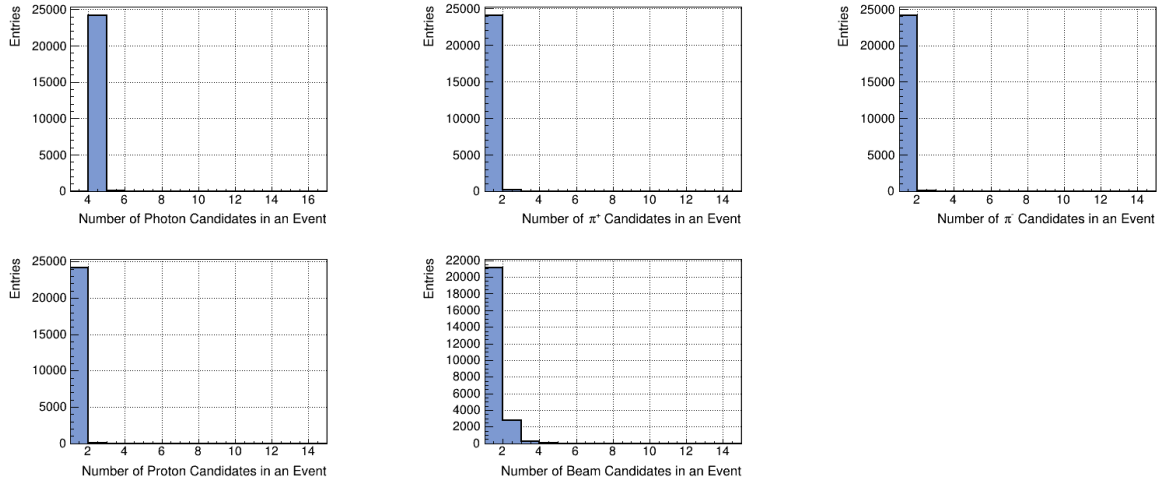


Figure 4.24: Number of particles in an event at this stage of the analysis. The primary source of extra combinations comes from extra beam candidates

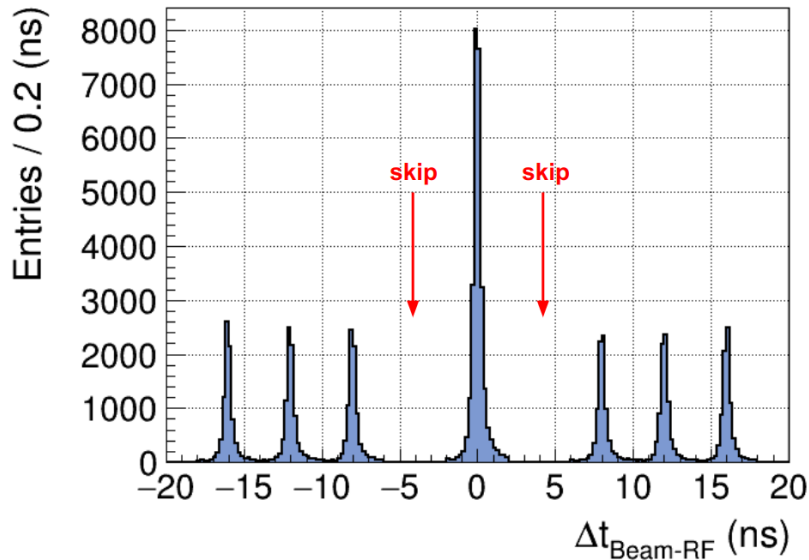


Figure 4.25: The accidentals are used for subtracting out-of-time photons that show up as in-time photons. The accidentals closest to the main peak are skipped to avoid over-subtracting events that lie within the tails of the in-time peak that bleed into these closest accidentals.

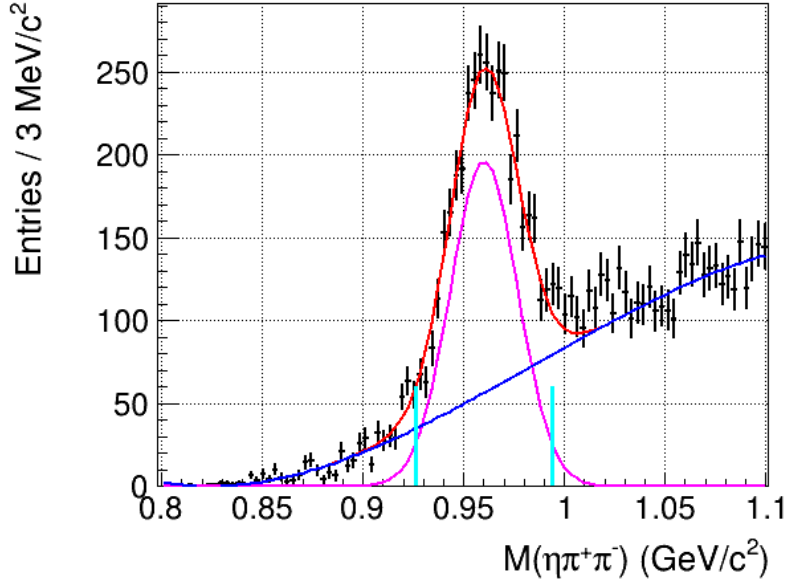


Figure 4.26: At this stage there is about 67% of the remaining $M(\eta\pi^+\pi^-)$ events that are signal considering a 2σ window using a Gaussian and polynomial background fit.

4.8.1 $\gamma p \rightarrow \eta' \eta p$

After performing the data selection, there is still a fair amount of background that remains under the peak of the η' . This is due to the background that was not subtracted out remaining under the η peaks. In fact, about 82% events are considered signal, while the remaining events are background considering the $M(2\gamma)$ for both of the η candidates Fig. 4.27.

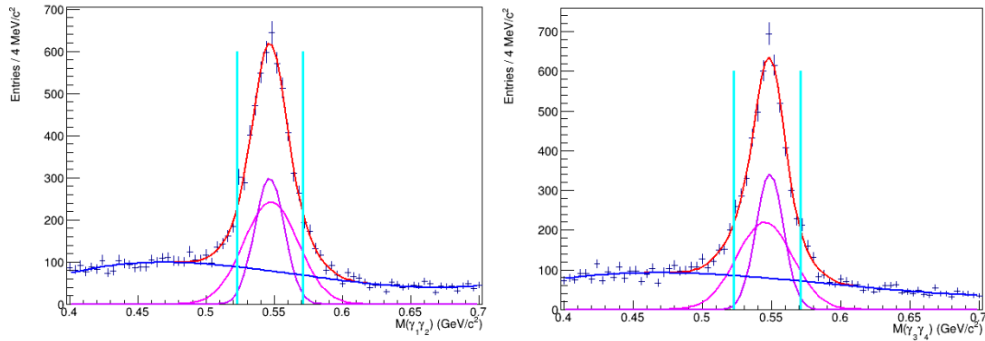


Figure 4.27: The $M(2\gamma)$ distributions have an estimated background of about 18% remaining under the η peak. This is used as a guide to understand how much background will be present in the constrained data set where the η masses are restricted to a δ peak at the η mass.

Now that the amount of background under the η s has been estimated after applying the data selection shown above, another step can be taken to improve the resolution and reduce the background under the η' . So far, the analysis files that have been used do not constrain the η masses. Combinations that lie within an η mass window of $(0.35, 0.75)$ GeV/c^2 are kept for both η candidates. However, analysis files that impose a kinematic constraint on the mass of the η s are accessible. Thus, a script was written that analyzes both the files that have the η masses unconstrained as well as the files that constrain the mass of the η s to be at the mass value given in [4]. Some of the events in the files that do not constrain the η masses do not show up in the constrained files because the kinematic fit did not converge for those events. After fitting the η' , the resolution is clearly improved using this method Fig. 4.29.

We have finally achieved an exclusive reaction of $\gamma p \rightarrow \eta' \eta p$. A complete list of data selections to get this stage is shown below Fig. 4.28. For the Fall 2018 run period, 1500 exclusive $\eta' \eta$ events were achieved. This analysis was extended to include the full GlueX Phase-I data set which includes also 2017 and 2018 Spring run periods. For the full GlueX Phase-I data, 4800 exclusive $\eta' \eta$ events were achieved which is the largest $\eta' \eta$ data set Fig. 4.30.

Name of the Cut	Events Kept
FCAL Photon Quality Factor	quality factor ≥ 0.5
Proton z Vertex	$52 \text{ cm} \leq z \leq 78 \text{ cm}$
π^0 Removal (Events) 3σ	$\gamma_i \gamma_j \leq 0.109 \text{ GeV}/c^2, \gamma_i \gamma_j \geq 0.161 \text{ GeV}/c^2$
Missing Mass Squared	$\text{MMS} < 0.04 $
Missing Energy	Events kept within 3σ region of the center of the ME distribution
Double η Selection 1.5σ	$0.521 \text{ GeV}/c^2 \leq \gamma_1 \gamma_2 \leq 0.584 \text{ GeV}/c^2$ $0.519 \text{ GeV}/c^2 \leq \gamma_3 \gamma_4 \leq 0.585 \text{ GeV}/c^2$
$M(\pi^+ \pi^-)$	$M(\pi^+ \pi^-) \leq 0.42 \text{ GeV}/c^2$
Beam Energy	$\text{BE} \geq 7.5 \text{ GeV}$
Confidence Level	$\text{CL} \geq 10^{-9}$
η' Selection	Events kept within 2σ region of η' for both η' candidates. For the overlap region of 2 η' s, $M(\eta \pi^+ \pi^-)$ closest to pdg value of η' mass kept
N(1535) Removal	$M(\eta p) > 1.65 \text{ GeV}/c^2$
Accidental Subtraction	Events weighted by $-\frac{1}{6}$ for out-of-time events

Figure 4.28: The final data selection criteria use to achieve an exclusive reaction of $\gamma p \rightarrow \eta' \eta p$.

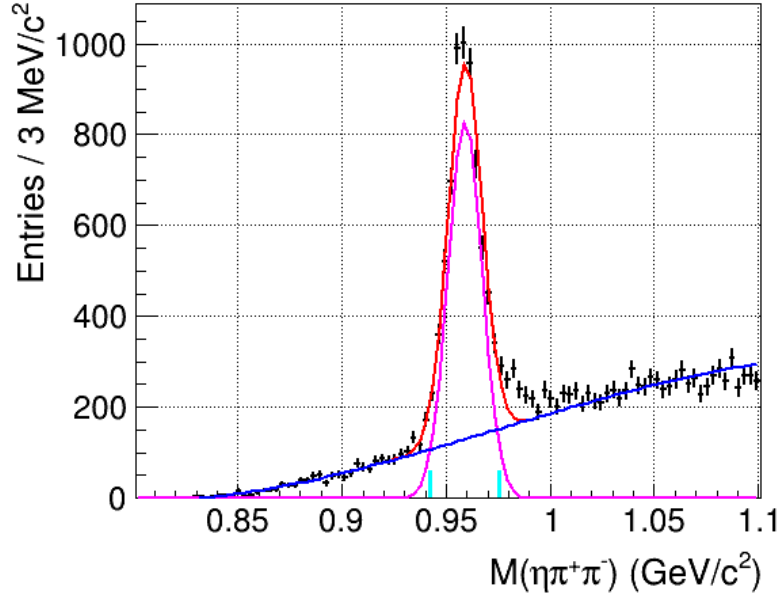


Figure 4.29: After matching the events that survive the kinematically fitted η s, the η' is fitted using the same methods previously. Using kinematically fitted η s clearly improves the resolution of the η' . This improves the signal percentage from 67% to 79%.

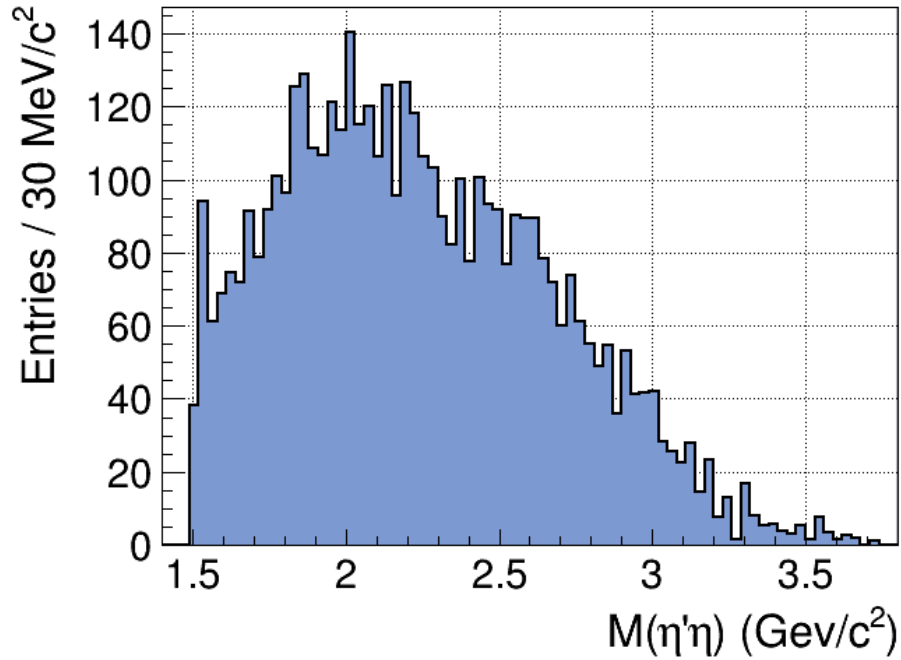


Figure 4.30: The final distribution $M(\eta\eta')$ after data selection. The mass distribution has an estimated 21% background remaining under the η' .

CHAPTER 5

OBSERVABLE: CROSS SECTION ESTIMATION

The cross section in particle physics is an observable that represents the probability of some reaction occurring. It is composed of the number of observed events of the reaction of interest normalized by the flux of the beam and the number of target particles taking into consideration the efficiency of the detector and the probability of the decay. The dimension of the cross section is area and is commonly given in units of barns. It can be thought of as the size of something that an incoming particle must hit for the production to occur. How well a detector is performing on an absolute scale can be gauged by the cross section. For this analysis, a differential cross section was measured. A differential cross section is measuring the cross section as a function of a variable such as beam energy, momentum transfer or invariant mass. For this analysis, a cross section as a function of the $M(\eta'\eta)$ was measured. This helps determine an estimate of an upper limit on how many $\eta'\eta$ events are produced in t-channel production. The cross section is calculated using the formula:

$$\sigma = \frac{N}{T * \Phi * Br * \epsilon}. \quad (5.1)$$

Where σ denotes the total cross section, N is the yield or total number events in the process, T is a target factor that denotes the number of target particles per cross sectional area, Φ is the beam flux, Br is the branching ratio, and ϵ is the efficiency of the detector. In this analysis, a differential cross section is measured. This quantity is just an extension of the cross section as a function of a kinematic variable. This analysis considered the differential cross section as a function of $M(\eta'\eta)$. An estimation of how the probability of the final state $\eta'\eta$ occurring from this reaction changes over the mass range can give us an idea for the upper bound of this production process. The differential cross section as a function of $M(\eta'\eta)$ is given by:

$$\frac{d\sigma}{dM} = \frac{N}{T * \Phi * Br * \epsilon * \Delta M}. \quad (5.2)$$

5.1 Yields

The total yield N is calculated by fitting the data using a Gaussian distribution to model the signal and a 3rd order polynomial to model the background. The number of signal and background events is calculated within a 2σ window. The yields have all data selections applied as discussed in the previous chapter including accidental subtraction. The differential cross section was calculated using four mass bins over the range of $M(\eta'\eta)$ Fig. 5.1. The first bin corresponds to the mass range 1.4 - 1.7 GeV/c^2 and has 519 ± 39 signal events. The second bin corresponds to the range 1.7 - 2.1 GeV/c^2 and has 1113 ± 52 signal events. The third bin corresponds to 2.1 - 2.5 GeV/c^2 and has 1708 ± 54 signal events. The fourth bin corresponds to 2.5 - 3.0 GeV/c^2 and has 1783 ± 52 signal events. Given below are the fits for the yields for each of these mass bins.

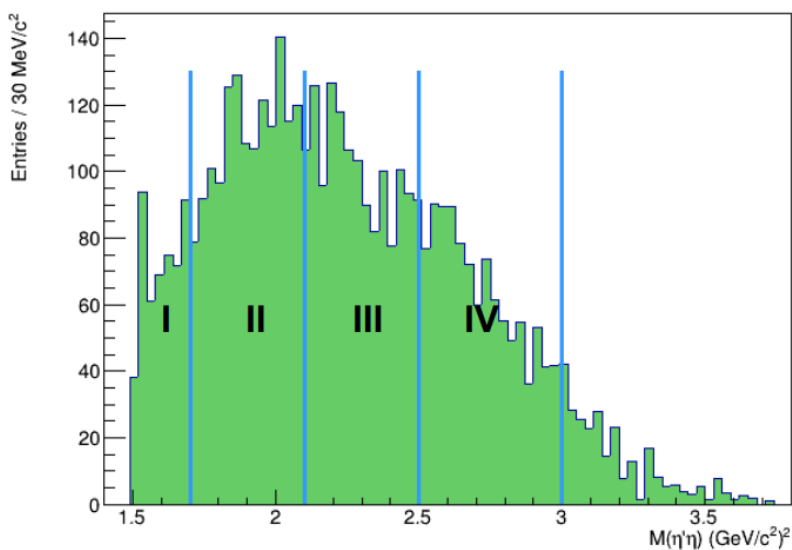


Figure 5.1: The $M(\eta'\eta)$ distribution split into bins of mass.

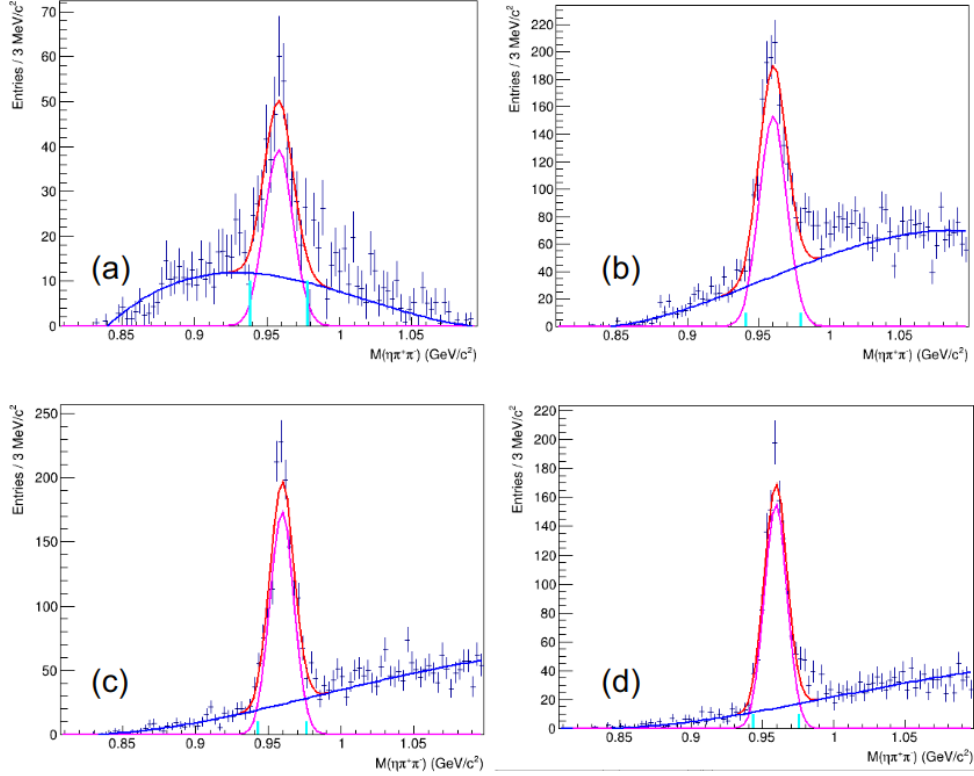


Figure 5.2: The yields for each $M(\eta\eta')$ bin are computed by fitting the $M(\eta\pi^+\pi^-)$ distribution with a Gaussian for the signal and a 3rd order polynomial for the background. The signal events are calculated using a 2σ window.

5.2 Target Factor

The target factor T can be thought of as how many target particles are present per cross sectional area. This factor can be calculated from the length of the target L and the density of the target ρ using N_A as Avogadro's number, and A as the molar mass through the formula:

$$T[\text{atoms}/\text{m}^2] = \frac{N_A[\text{atoms}/\text{mol}] * L[\text{m}] * \rho[\text{kg}/\text{m}^3]}{A[\text{kg}/\text{mol}]} \quad (5.3)$$

For the GlueX experiment, the factor is calculated to be $1.22 \times 10^{-28} \text{m}^{-2}$ in SI units or 1.22b^{-1} where b is the unit of barns which is used frequently to describe units of cross section.

5.3 Flux

The flux from the beam Φ is measured by the pair spectrometer. A script located on the GlueX GitHub repositories attains the flux values for a certain beam energy range and a certain run range

for a specified run period. For the total GlueX Phase-I data, the flux values are averaged over each of the total run periods for the 2017 and 2018 run periods described in the Data/Software versions section. The run number ranges are given in Fig. 4.1.

5.4 Branching Fraction

The Branching Fraction Br is obtained from the Particle Data Group particle listings [4]. The final state of this reaction is $\eta'\eta$ where $\eta' \rightarrow \eta\pi^+\pi^-$ and each $\eta \rightarrow 2\gamma$. The branching fraction for $\eta' \rightarrow \eta\pi^+\pi^-$ is $42.5 \pm 0.7\%$ and the branching fraction for $\eta \rightarrow 2\gamma$ is $39.36 \pm 0.2\%$. We must have one process of $\eta' \rightarrow \eta\pi^+\pi^-$ and two processes of $\eta \rightarrow 2\gamma$. We multiply these together and use the rule of combining uncertainties to get an overall branching fraction of $6.58 \pm 0.18\%$.

5.5 Monte Carlo Efficiency

The next step is determining the efficiency ϵ from Monte Carlo simulation. The particles must pass through the detector and be reconstructed after surviving the selection criteria at the data selection stage. Thus, the MC efficiency includes both the acceptance and the efficiency of the detector. To calculate this, reconstructed MC events that pass all the selection cuts are divided by the generated events. This is calculated for the different run periods as shown below. The total efficiency for GlueX Phase-I is determined by summing each of the efficiencies for the run periods weighted by how much each contributes to the total Phase-I yield.

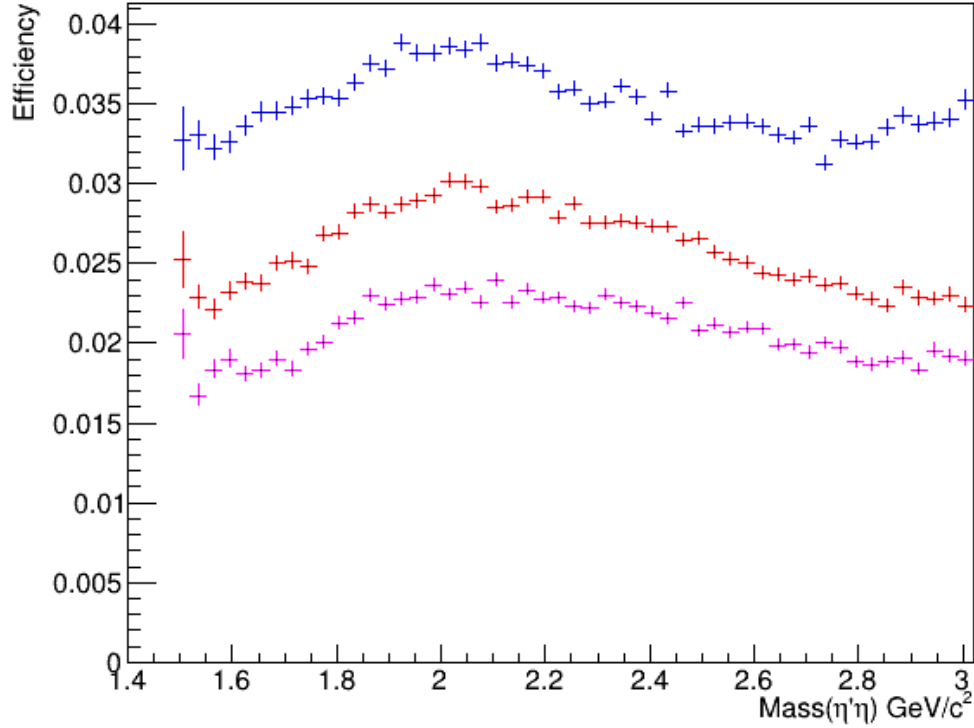


Figure 5.3: The Monte Carlo efficiencies as a function of $M(\eta'\eta)$. The efficiency is calculated by dividing the accepted MC over the generated MC. The efficiency for the 2017 run period is given in blue, the efficiency for the 2018-01 run period is given in red, and the efficiency for the 2018-08 run period is given in magenta.

5.6 Differential Cross Section

Finally, the ΔM corresponds to binning the cross section in bins of $M(\eta'\eta)$. This gives more information on the physics of the reaction at different ranges of mass. For this analysis, four bins of mass were used corresponding to the regions $(1.4, 1.7) \text{ GeV}/c^2$, $(1.7, 2.1) \text{ GeV}/c^2$, $(2.1, 2.5) \text{ GeV}/c^2$, and $(2.5, 3.0) \text{ GeV}/c^2$ Fig. 5.1. The uncertainties shown are statistical uncertainties. The data used is the entire GlueX Phase-I data set. This is the first observable measurement for this final state reaction in photo-production.

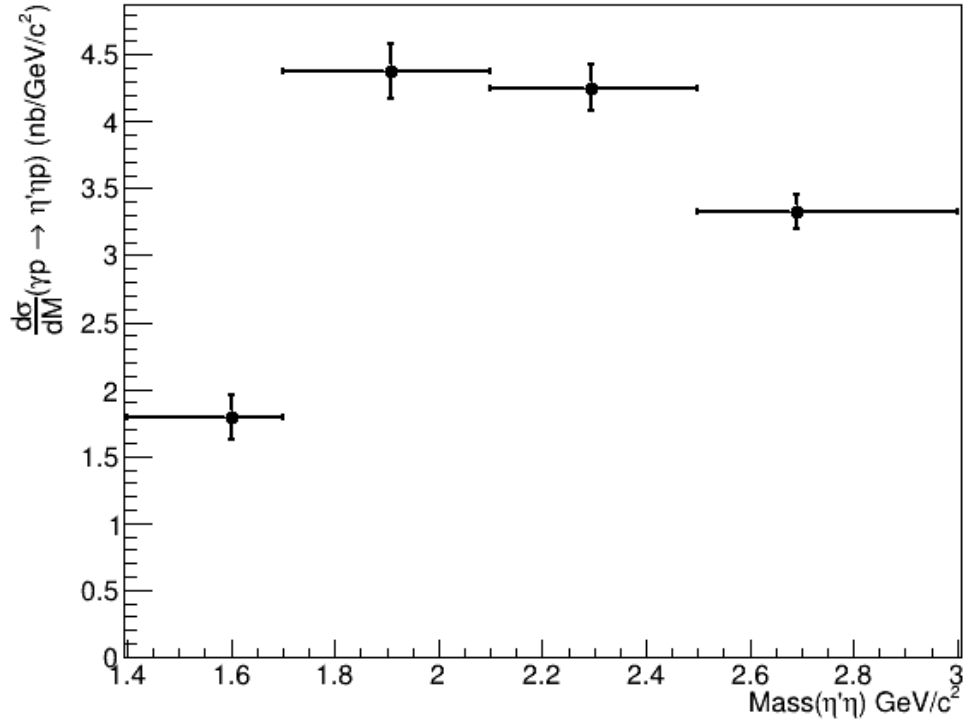


Figure 5.4: The differential cross section in bins of $M(\eta'\eta)$. Statistical uncertainties are shown.

CHAPTER 6

SYSTEMATICS

A few studies were performed to understand where contributions to systematic uncertainties in the measurement arise from. The main focus was to test how event selections perform on data versus the effect on simulations. The studies will be presented with conclusions to follow.

6.1 The Barlow Test of Significance

The Barlow test of significance is used in this analysis to test the effects of varying certain data selection criteria. R. Barlow describes the process in his paper in detail [51]. A nominal measurement can be defined as having a value of x with a statistical standard deviation of σ_x . If a variation is performed, in this case varying one of the data selections slightly while keeping all the others constant, the variation measurement will produce a value y with statistical standard deviation σ_y . The values and standard deviations should be similar since only one data selection is varied while the others are kept the same. In order to measure the degree of variation, the quantity $\frac{|\Delta|}{\sigma_\Delta}$ is calculated. If $\frac{|\Delta|}{\sigma_\Delta}$ is larger than 4 then the variation should be included in the systematic uncertainty. There are three data selections that will be tested using this method: The selection of two η s, the η' selection, and the removal of the N(1535) resonance. For each of these data selections, one looser selection and two tighter cuts are performed and compared with the nominal selection.

6.1.1 Systematic Study of the Selection of Two η s

As mentioned earlier, there is still 18% background remaining under the peak for the two η s. After testing a variety of selections, a choice was made on the nominal selection of 1.5σ . Using the Barlow significance method, a looser selection of 2σ as well as two tighter selections of 1σ and 1.5σ were made. All other data selection criteria mentioned in the above data selection studies were performed with no deviations such that the η selection was the only selection that was varied. The differential cross section was calculated for each of these variations and can be seen on the plot below including their statistical uncertainties Fig. 6.1. From this, $\frac{\Delta}{\sigma_\Delta}$ was calculated referencing the nominal value and is plotted as a function of the $M(\eta'\eta)$ Fig. 6.2.

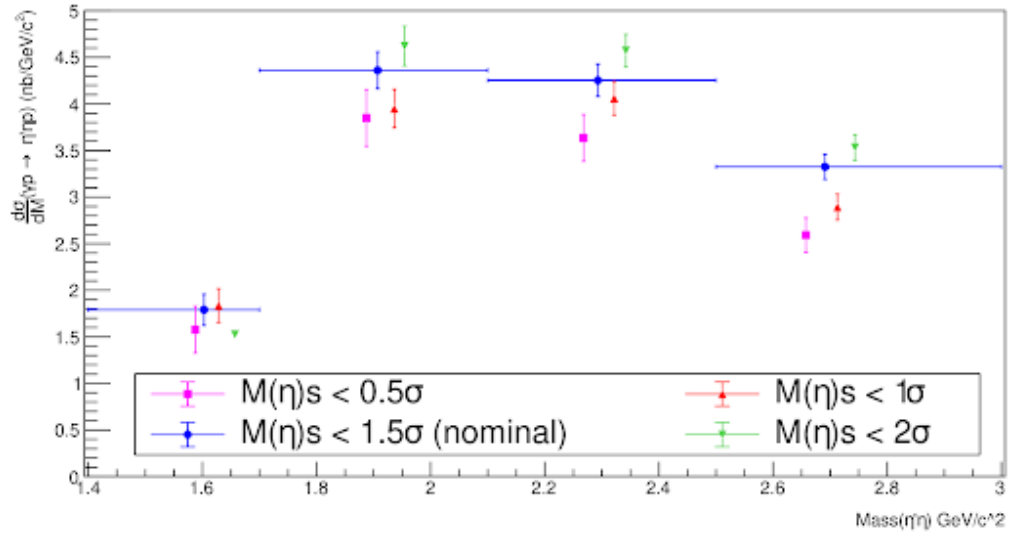


Figure 6.1: The differential cross section in bins of $M(\eta'\eta)$ for different η selections.

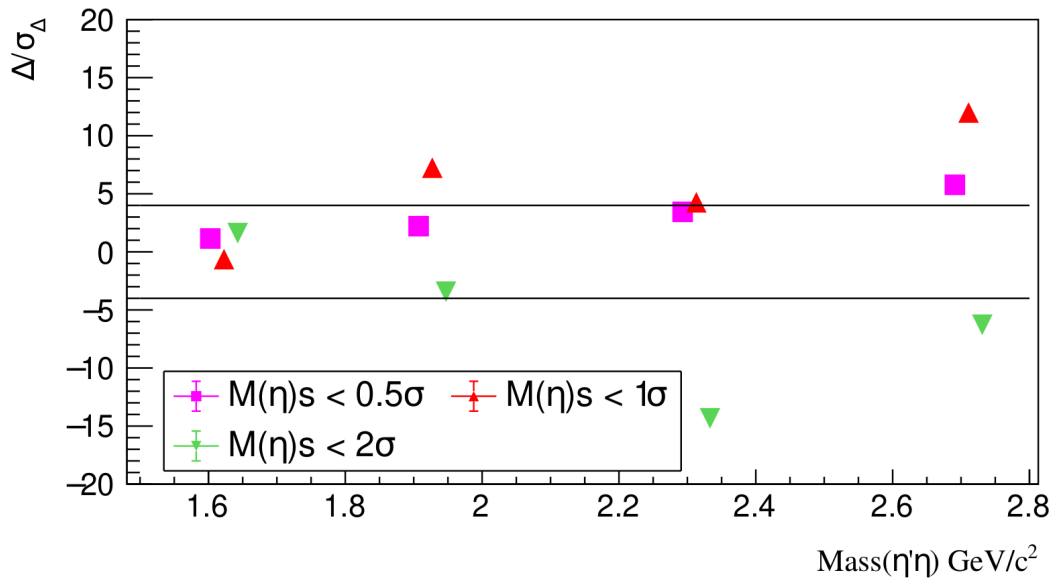


Figure 6.2: Plotted is Δ/σ_Δ , the significance for the Barlow test, in bins of $M(\eta'\eta)$ for different η selections.

6.1.2 Systematic Study of the Selection of η'

The nominal η' selection of as mentioned in the data selection procedure was chosen to be a 2σ selection. Following the same procedure as was carried out for the η selection, a looser selection of 2.5σ as well as two tighter selections of 1.5σ and 1σ were made, varying only this selection and holding the rest constant. The differential cross section was calculated for each of these variations and can be seen on the plot below including their statistical uncertainties Fig. 6.3. From this, $\frac{\Delta}{\sigma_{\Delta}}$ was calculated referencing the nominal value and is plotted as a function of the $M(\eta'\eta)$ Fig. 6.4

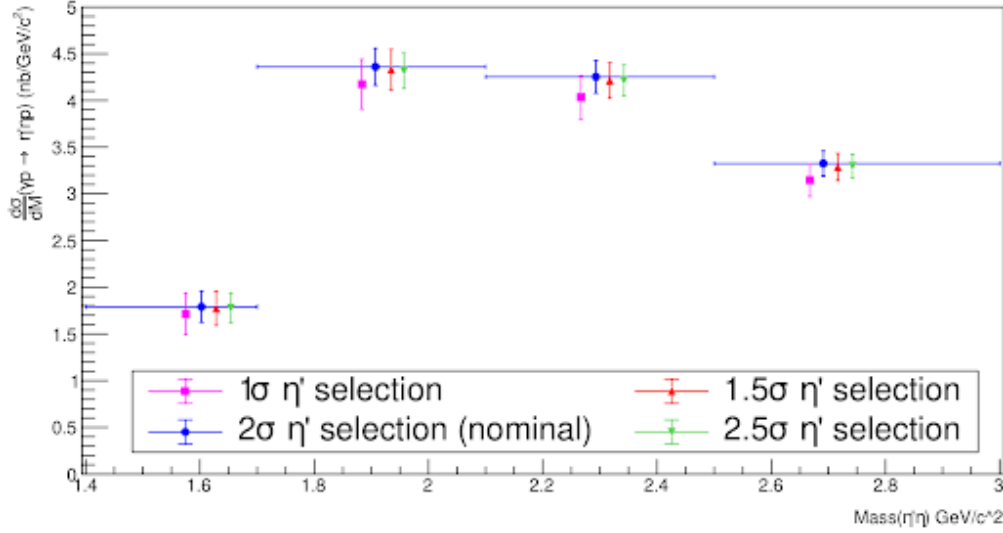


Figure 6.3: The differential cross section in bins of $M(\eta'\eta)$ for different η' selections.

6.1.3 Systematic Study of the Removal of the N(1535)

The nominal selection on the $M(\eta p)$ to remove the N(1535) was chosen to be $M(\eta p) \geq 1.65$ GeV/c². This selection was varied following the Barlow criteria where a looser selection choosing $M(\eta p) \geq 1.60$ GeV/c² as well as two tighter selections choosing $M(\eta p) \geq 1.70$ GeV/c² and $M(\eta p) \geq 1.75$ GeV/c² were made. The differential cross section was calculated for each of these variations and can be seen on the plot below including their statistical uncertainties Fig. 6.5. From this, $\frac{\Delta}{\sigma_{\Delta}}$ was calculated referencing the nominal value and is plotted as a function of the $M(\eta'\eta)$ Fig. 6.6

A summary is given below of the systematic uncertainties in different mass bins TAB. 6.1

After performing the Barlow significance test, the η selection and removal of the N(1535) are the two selections that show significance. The values for the significance for the different η' ranges all lie between -4 and 4 and is therefore not necessary to include in systematic uncertainties. For

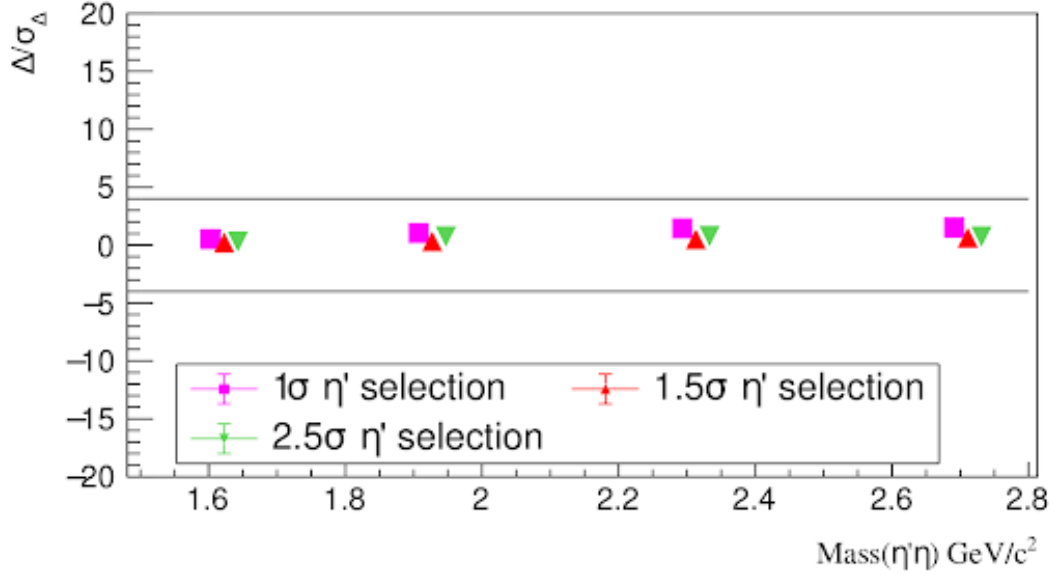


Figure 6.4: Plotted is Δ/σ_{Δ} , the significance for the Barlow test, in bins of $M(\eta'\eta)$ for different η' selections.

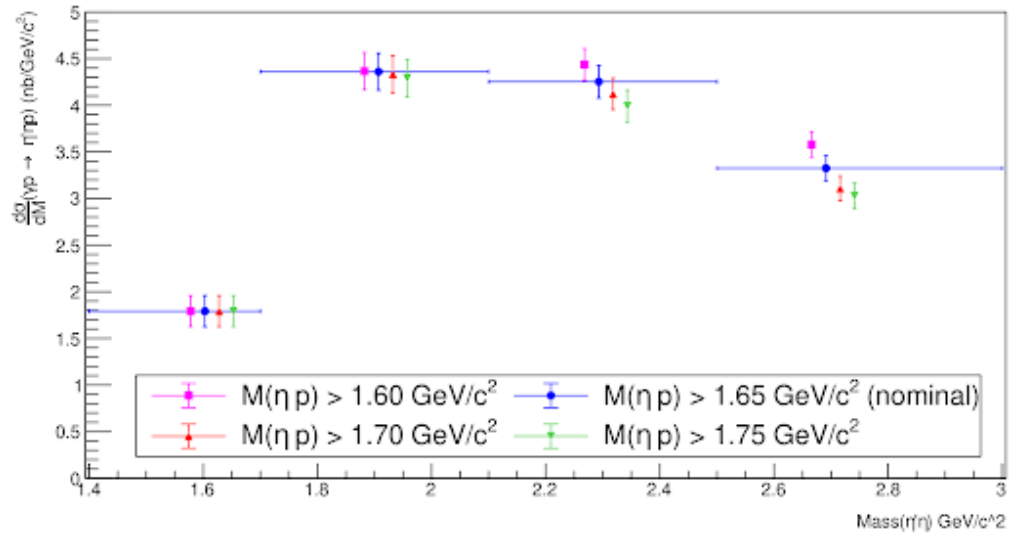


Figure 6.5: The differential cross section in bins of $M(\eta'\eta)$ for different $M(\eta p)$ selections.

the η selection and the N(1535) removal, the significance values that are farthest from zero are chosen for each and the corresponding Δ values for these are used for the systematic uncertainties. The final differential cross section with both statistical and systematic uncertainties is shown below Fig. 6.7.

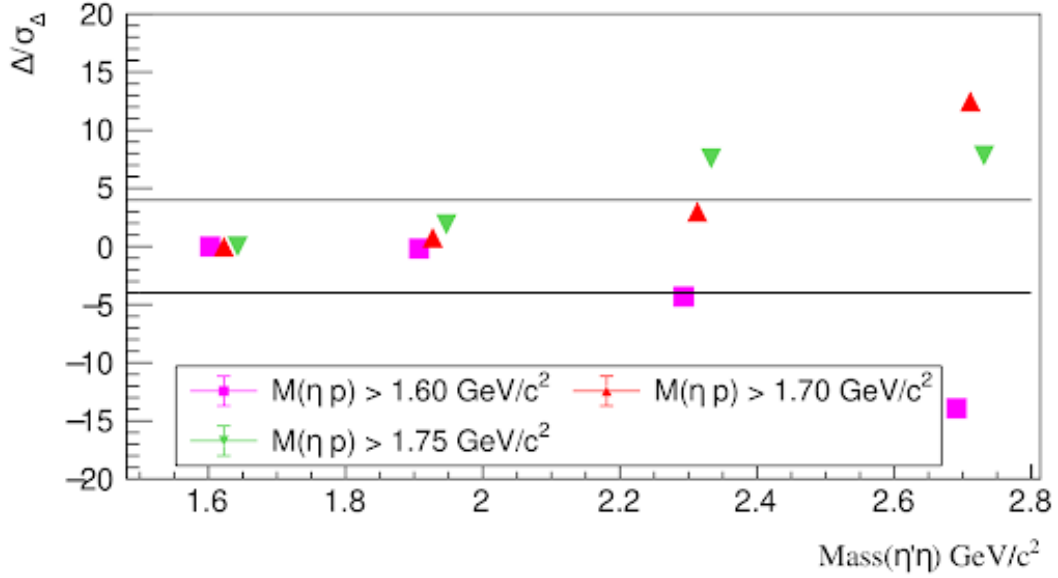


Figure 6.6: Plotted is Δ/σ_Δ , the significance for the Barlow test, in bins of $M(\eta'\eta)$ for different $M(\eta p)$ selections.

Table 6.1: Table of systematics for each mass bin and variation where Δ/σ_Δ , the significance, is either greater than 4 or less than -4. σ_Δ is the difference between the differential cross section of the variation and the nominal in units of microbarns/ GeV^2 .

$M(\eta'\eta)$ GeV/c^2	Variation	Δ/σ_Δ	σ_Δ
$1.7 \leq M(\eta'\eta) \leq 2.1$	1σ η selection	7.24584	0.0566661
$2.1 \leq M(\eta'\eta) \leq 2.5$	1σ η selection	4.26903	0.0450577
$2.1 \leq M(\eta'\eta) \leq 2.5$	2σ η selection	-14.3332	0.0222418
$2.1 \leq M(\eta'\eta) \leq 2.5$	$M(\eta p) \geq 1.75$	7.56066	0.0345024
$2.1 \leq M(\eta'\eta) \leq 2.5$	$M(\eta p) \geq 1.60$	-4.30809	0.0426755
$2.5 \leq M(\eta'\eta) \leq 3.0$	0.5σ η selection	5.77379	0.126949
$2.5 \leq M(\eta'\eta) \leq 3.0$	1σ η selection	11.9972	0.0360443
$2.5 \leq M(\eta'\eta) \leq 3.0$	2σ η selection	-6.27849	0.0329767
$2.5 \leq M(\eta'\eta) \leq 3.0$	$M(\eta p) \geq 1.75$	7.80838	0.0380919
$2.5 \leq M(\eta'\eta) \leq 3.0$	$M(\eta p) \geq 1.70$	12.4914	0.0174524
$2.5 \leq M(\eta'\eta) \leq 3.0$	$M(\eta p) \geq 1.65$	-13.9119	0.0182261

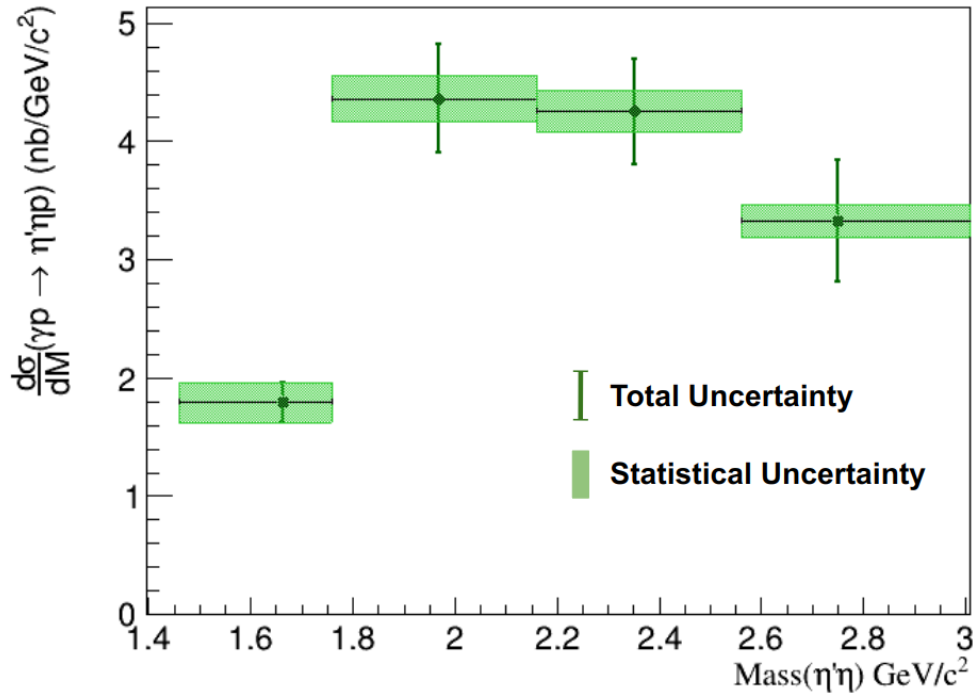


Figure 6.7: The differential cross section in bins of $M(\eta'\eta)$. Statistical uncertainties are shown with the light green shaded blocks. The total uncertainty is the systematic uncertainty added in quadrature with the statistical uncertainty and is shown by the dark green error bars.

CHAPTER 7

FUTURE OUTLOOK AND CONCLUSION

The limited statistics for this channel has proven to be quite a challenge. GlueX Phase-II is underway and is expected to increase statistics by two or three times. As was mentioned previously, there is still background remaining under the η peaks that has not been subtracted out. This will not affect the differential cross section since the η' was fitted, however it will show up in the mass distribution of $\eta'\eta$. One method to handle this background is using sideband subtraction. This method estimates the background present under the signal peak by using regions to the left and right of the signal. The signal region is then weighted by negative weights corresponding to this background estimation. The reason that this analysis did not implement a sideband subtraction was due to the limited statistics and the challenge of acquiring sufficient fits for the yields in the different mass bins to calculate the cross section.

Another method of subtracting out remaining background would be to focus on the η' . There is 21% background remaining under the η' peak. One way to handle this background is using a technique called Q-factor weighting. Q-factor weighting is a multivariate sideband subtraction of the data using probabilistic weights [52]. The idea is that the phase space of a reaction can be determined by some set of coordinates and a subset can be chosen for referencing in a region where the signal and background are well understood. For the region where the non-reference coordinates exist, a number of nearest neighbors are calculated using a metric and an unbinned maximum likelihood fit is performed for each reference coordinate on the nearest neighbors. The value for the Q-factor is given by the fraction of the signal or probability from the fit results. This is used for weighting each event.

Another future path for this channel is to calculate an observable called the beam asymmetry. Measuring this can give information on possible production mechanisms for the reaction. Further studies can also improve systematics. The η' was fitted using a Gaussian distribution where the background was modeled as a 3rd order polynomial. Using a different order polynomial or varying the fit range and calculating the yields can give an estimation on how sensitive the fits are in the calculation of the yields. Testing different fit functions for signal and background distributions can help minimize the statistical uncertainties as well.

This analysis is the first ever study for photoproduction of the final state $\eta\eta'$. Data selections were performed for the full GlueX Phase-I data set to achieve the reaction for $\gamma p \rightarrow \eta'\eta p$. A preliminary differential cross section measurement was performed in bins of mass of $\eta\eta'$ for four different mass bins to estimate t-channel production of this final state. At this stage there is no significant evidence for an isoscalar hybrid state in this mass spectrum. The comparison with BESIII results agrees with the rise near threshold and the peak near $2.0 \text{ GeV}/c^2$, however there is a significant dip in the BESIII results that is not observed in this analysis. This could be due to remaining 21% background that is not subtracted out from the η' or it is possible that it could be due to the other isoscalar resonance that is expected to decay to $\eta'\eta$, namely, the η'_1 . Further studies are necessary to explore this and adding GlueX Phase-II data will help illuminate more exciting information that has yet to be discovered.

BIBLIOGRAPHY

- [1] David Griffiths. *Introduction to elementary particles*. John Wiley & Sons, 2020.
- [2] Wikimedia Commons. Standard model of elementary particles, 2019.
- [3] Siegfried Bethke. Experimental tests of asymptotic freedom. *Progress in particle and Nuclear Physics*, 58(2):351–386, 2007.
- [4] Masaharu Tanabashi, K Hagiwara, K Hikasa, K Nakamura, Y Sumino, F Takahashi, J Tanaka, K Agashe, G Aielli, C Amsler, et al. Review of particle physics (rpp2018). *Physical Review D*, 98(3):1–1898, 2018.
- [5] Jozef J Dudek, Robert G Edwards, Peng Guo, Christopher E Thomas, Hadron Spectrum Collaboration, et al. Toward the excited isoscalar meson spectrum from lattice qcd. *Physical Review D*, 88(9):094505, 2013.
- [6] C Adolph, R Akhunzyanov, MG Alexeev, GD Alexeev, A Amoroso, V Andrieux, V Anosov, A Austregesilo, B Badelek, F Balestra, et al. Odd and even partial waves of η meson: math altimg=. *Physics Letters B*, 740:303–311, 2015.
- [7] DV Amelin, Yu G Gavrilo, Yu P Gouz, VA Dorofeev, RI Dzhelyadin, AM Zaitsev, AV Zenin, AV Ivashin, IA Kachaev, VV Kabachenko, et al. Investigation of hybrid states in the ves experiment at the institute for high energy physics (protvino). *Physics of Atomic Nuclei*, 68:359–371, 2005.
- [8] EI Ivanov, DL Stienike, DI Ryabchikov, GS Adams, T Adams, Z Bar-Yam, JM Bishop, VA Bodyagin, DS Brown, NM Cason, et al. Observation of exotic meson production in the reaction $\pi^- p \rightarrow \eta \pi^- p$ at 18 gev/c. *Physical review letters*, 86(18):3977, 2001.
- [9] M Ablikim, MN Achasov, P Adlarson, S Ahmed, M Albrecht, R Aliberti, A Amoroso, MR An, Q An, XH Bai, et al. Observation of an isoscalar resonance with exotic $J^PC = 1^{--}$ quantum numbers in $J/\psi \rightarrow \gamma \eta \eta'$. *Physical Review Letters*, 129(19):192002, 2022.
- [10] Jefferson Lab | Flickr. <https://www.flickr.com/photos/jeffersonlab/>.
- [11] Photos | gluexweb.jlab.org. <https://gluexweb.jlab.org/photos/>.
- [12] H Al Ghou, EG Anassontzis, A Austregesilo, F Barbosa, A Barnes, TD Beattie, DW Bennett, VV Berdnikov, T Black, W Boeglin, et al. Measurement of the beam asymmetry σ for π^0 and η photoproduction on the proton at $e\gamma = 9$ gev. *Physical Review C*, 95(4):042201, 2017.
- [13] Joseph John Thomson. *Cathode rays*. Number 4. Academic Reprints, 1897.

- [14] James G O'Hara. George johnstone stoney, frs and the concept of the electron. *Notes and Records of the Royal Society of London*, 29(2):265–276, 1975.
- [15] JJ Thomson FRS XXIV. On the structure of the atom: an investigation of the stability and periods of oscillation of a number of corpuscles arranged at equal intervals around the circumference of a circle; with application of the results to the theory of atomic structure. *The London, Edinburgh, and Dublin Philosophical Magazine and Journal of Science*, 7(39):237–265, 1904.
- [16] Ernest Rutherford. Lxxix. the scattering of α and β particles by matter and the structure of the atom. *The London, Edinburgh, and Dublin Philosophical Magazine and Journal of Science*, 21(125):669–688, 1911.
- [17] Niels Bohr. Om brintspektret. *Fysisk Tidsskrift*, 12:97–114, 1914.
- [18] Niels Bohr. *The theory of spectra and atomic constitution*. CUP Archive, 1924.
- [19] James Chadwick. The neutron. *Bakerian Lecture*, *Proc. Roy. Soc. Lon*, 142:1–25, 1933.
- [20] A. Einstein. Über einen die erzeugung und verwandlung des liches betreffenden heuristischen gesichtspunkt. *Annalen der Physik*, 322(6):132–148, 1905.
- [21] Arthur H Compton. Wave-length measurements of scattered x-rays. *Physical Review*, 21(6):715, 1923.
- [22] Laurie M Brown. Hideki yukawa and the meson theory. *Physics Today*, 39(12):55–62, 1986.
- [23] Celso MG LATTES, Hugh Muirhead, Giuseppe PS Occhialini, and Cecil Frank Powell. Processes involving charged mesons. *Nature*, 159(4047):694–697, 1947.
- [24] M Gell-Mc. 11711. a schematic model of ba, ryons and mesons. *Physics Letters, S (3)*, 214, 1964.
- [25] George Zweig. An su ₃ model for strong interaction symmetry and its breaking. Technical report, CM-P00042884, 1964.
- [26] Atlas Collaboration, Georges Aad, T Abajyan, B Abbott, J Abdallah, S Abdel Khalek, Ahmed Ali Abdelalim, O Abidinov, R Aben, B Abi, et al. A particle consistent with the higgs boson observed with the atlas detector at the large hadron collider. *Science*, 338(6114):1576–1582, 2012.
- [27] Frank E Close. Introduction to quarks and partons. 1979.
- [28] T Barnes, N Black, and PR Page. Strong decays of strange quarkonia. *Physical Review D*, 68(5):054014, 2003.

- [29] Neal M Cason and E852 Collaboration. Exotic meson production in the reaction $\pi - p \rightarrow \eta$ / $\pi - p$ at 18 gev/c. In *AIP Conference Proceedings*, volume 549, pages 318–321. American Institute of Physics, 2000.
- [30] Hermann A Grunder, JJ Bisognano, WI Diamond, BK Hartline, CW Leemann, Jean Mougey, RM Sundelin, and RC York. The continuous electron beam accelerator facility. *Nuclear Physics A*, 478:831–846, 1988.
- [31] Reza Kazimi, Kevin Beard, Jay Benesch, Arne Freyberger, Joseph Grames, Tommy Hiatt, Geoffrey Krafft, Nikolitsa Merminga, B Poelker, M Spata, et al. Cebaf injector achieved world’s best beam quality for three simultaneous beam with a wide range of bunch charges. Technical report, Thomas Jefferson National Accelerator Facility (TJNAF), Newport News, VA . . . , 2004.
- [32] S Adhikari, CS Akondi, H Al Ghouli, A Ali, M Amaryan, EG Anassontzis, A Austregesilo, F Barbosa, J Barlow, A Barnes, et al. The gluex beamline and detector. *Nuclear Instruments and Methods in Physics Research Section A: Accelerators, Spectrometers, Detectors and Associated Equipment*, 987:164807, 2021.
- [33] Michael Dugger, BG Ritchie, N Sparks, K Moriya, RJ Tucker, RJ Lee, BN Thorpe, T Hodges, FJ Barbosa, N Sandoval, et al. Design and construction of a high-energy photon polarimeter. *Nuclear Instruments and Methods in Physics Research Section A: Accelerators, Spectrometers, Detectors and Associated Equipment*, 867:115–127, 2017.
- [34] Kjell J Mork. Pair production by photons on electrons. *Physical Review*, 160(5):1065, 1967.
- [35] F Barbosa, C Hutton, Alexandre Sitnikov, A Somov, S Somov, and Ivan Tolstukhin. Pair spectrometer hodoscope for hall d at jefferson lab. *Nuclear Instruments and Methods in Physics Research Section A: Accelerators, Spectrometers, Detectors and Associated Equipment*, 795:376–380, 2015.
- [36] D Hall. Superconducting solenoid-technical note, mar 2018.
- [37] CD Keith. Halld lh2 cryotarget, jan 2014.
- [38] Eric Pooser, Fernando Barbosa, Werner Boeglin, Charles Hutton, MM Ito, Mahmoud Kamel, Puneet Khetarpal, Anthony Llodra, N Sandoval, Simon Taylor, et al. The gluex start counter detector. *Nuclear Instruments and Methods in Physics Research Section A: Accelerators, Spectrometers, Detectors and Associated Equipment*, 927:330–342, 2019.
- [39] Curtis A Meyer and Yves van Haarlem. Hall d tracking and pid review. 2008.
- [40] NS Jarvis, CA Meyer, B Zihlmann, M Staib, A Austregesilo, F Barbosa, C Dickover, V Razmyslovich, S Taylor, Y Van Haarlem, et al. The central drift chamber for gluex. *Nuclear Instruments and Methods in Physics Research Section A: Accelerators, Spectrometers, Detectors and Associated Equipment*, 962:163727, 2020.

- [41] L Pentchev, F Barbosa, V Berdnikov, D Butler, S Furletov, L Robison, and B Zihlmann. Studies with cathode drift chambers for the gluex experiment at jefferson lab. *Nuclear Instruments and Methods in Physics Research Section A: Accelerators, Spectrometers, Detectors and Associated Equipment*, 845:281–284, 2017.
- [42] Lubomir Pentchev, Benedikt Zihlmann, and GlueX collaboration. Forward drift chamber for the gluex experiment at the 12 gev cebaf machine. In *AIP Conference Proceedings*, volume 1336, pages 565–568. American Institute of Physics, 2011.
- [43] Tegan D Beattie, AM Foda, CL Henschel, S Katsaganis, ST Krueger, GJ Lolos, Zisis Pappandreou, EL Plummer, IA Semenova, A Yu Semenov, et al. Construction and performance of the barrel electromagnetic calorimeter for the gluex experiment. *Nuclear Instruments and Methods in Physics Research Section A: Accelerators, Spectrometers, Detectors and Associated Equipment*, 896:24–42, 2018.
- [44] RR Crittenden, AR Dzierba, J Gunter, R Lindenbusch, DR Rust, E Scott, PT Smith, T Sulanke, S Teige, BB Brabson, et al. A 3000 element lead-glass electromagnetic calorimeter. *Nuclear Instruments and Methods in Physics Research Section A: Accelerators, Spectrometers, Detectors and Associated Equipment*, 387(3):377–394, 1997.
- [45] Kei Moriya, John P Leckey, Matthew R Shepherd, Kevin Bauer, Daniel Bennett, H Egiyan, J Frye, J Gonzalez, SJ Henderson, D Lawrence, et al. A measurement of the energy and timing resolution of the gluex forward calorimeter using an electron beam. *Nuclear Instruments and Methods in Physics Research Section A: Accelerators, Spectrometers, Detectors and Associated Equipment*, 726:60–66, 2013.
- [46] M Dugger et al. Hall d/gluex technical construction report. Technical report, Chapter 3.10, Tech. rep., Jefferson Lab, Technical Report GlueX-doc-2511 . . . , 2017.
- [47] M Dugger, B Ritchie, I Senderovich, E Anassontzis, P Ioannou, C Kourkouveli, G Vasileiadis, G Voulgaris, N Jarvis, W Levine, et al. A study of decays to strange final states with gluex in hall d using components of the babar dirc. *arXiv preprint arXiv:1408.0215*, 2014.
- [48] D Lersch. The gluex kinematic fitter in 20 min. *GlueX-doc-5592 May*, 2022.
- [49] P Mattione. Least squares kinematic fitting of physics reactions. *GlueX-doc-2112, April*, 2016.
- [50] A Austregesilo. Task force report:vertex recoil proton event selection. *GlueX-doc-4924, February*, 2021.
- [51] Roger Barlow. Systematic errors: facts and fictions. *arXiv preprint hep-ex/0207026*, 2002.
- [52] M Williams, M Bellis, and CA Meyer. Multivariate side-band subtraction using probabilistic event weights. *Journal of Instrumentation*, 4(10):P10003, 2009.

BIOGRAPHICAL SKETCH

Jason was born and raised in a small town called Waxhaw, North Carolina. In 2014 he graduated from North Carolina State University with a bachelor of arts degree in Physics and a bachelor of science with honors in Mathematics. He continued his education at the University of North Carolina at Charlotte and received a masters degree in Applied Physics in 2016. He joined Florida State University in the fall of 2016 to pursue a PhD. He started working with Paul Eugenio and the Jefferson Lab's GlueX experiment in 2017 to conduct research on the search for exotic hybrid mesons.